Chapter 4

Seismic structure in southern Peru: Evidence for a smooth contortion between flat and normal subduction of the Nazca plate

4.1 Abstract

Rapid changes in slab geometry are typically associated with fragmentation of the subducted plate; however, continuous curvature of the slab is also possible. The transition from flat to normal subduction in southern Peru is one such geometrical change. The morphology of the subducted Nazca plate along this transition is explored using intraslab earthquakes recorded by temporary regional seismic arrays. Observations of a gradual increase in slab dip coupled with a lack of any gaps or vertical offsets in the intraslab seismicity suggest a smooth contortion of the slab. Concentrations of focal mechanisms at orientations which are indicative of slab bending are also observed along the change in slab geometry. The presence of a thin ultra-slow velocity layer (USL) atop the horizontal Nazca slab is identified and located. The lateral extent of this USL is coincident with the margin of the projected linear continuation of the subducting Nazca Ridge, implying a causal relationship. Waveform modeling of the 2D structure in southern Peru using a finite-difference algorithm provides constraints on the velocity and geometry of the slab's seismic structure and confirms the absence of any tears in the slab. The seismic and structural evidence suggests smooth contortion of the Nazca

plate along the transition from flat to normal subduction. The slab is estimated to have experienced 10% strain in the along-strike direction across this transition.

4.2 Introduction

The transition from flat to normal subduction may be accommodated by either a tear in the slab, as has been suggested in western (*Bandy et al.*, 2000; *Dougherty et al.*, 2012; *Stubailo et al.*, 2012) and eastern (*Dougherty and Clayton*, 2014) central Mexico, or a smooth contortion, such as that imaged in central Chile (*Pesicek et al.*, 2012). Here, we investigate the slab morphology across such a transition in southern Peru, where the Nazca plate is subducting beneath the South American plate at a convergence rate of ∼7.1 cm/yr along an azimuth of N77°E (*DeMets et al.*, 2010) (Figure 4.1). In the flat subduction region located north of ∼15°S, the slab dips at ∼30° near the trench to a depth of 100 km, then continues horizontally for ∼300 km before dipping steeply into the mantle (*Hasegawa and Sacks*, 1981; *Cahill and Isacks*, 1992). In the normal subduction region to the south, the slab dips at a constant ∼30° to at least 300 km depth (*Hasegawa and Sacks*, 1981; *Cahill and Isacks*, 1992). Previous studies of this transition region have suggested both tearing (e.g., *Barazangi and Isacks*, 1976, 1979; *Yamaoka et al.*, 1986) and continuous curvature (e.g., *Hasegawa and Sacks*, 1981; *Bevis and Isacks*, 1984; *Boyd et al.*, 1984; *Grange et al.*, 1984a; *Cahill and Isacks*, 1992; *Phillips and Clayton*, 2014) of the subducted Nazca plate. The approximate spatial coincidence of the subducting Nazca Ridge (*Barazangi and Isacks*, 1976, 1979) and the regional scale inflection in the shape of the western edge of the South American plate (*Bevis and Isacks*, 1984) with the transition in slab dip (Figure 4.2) has been used to identify possible causes of tearing or contortion, respectively, of the plate. The Nazca Ridge has been proposed to act as a line of weakness along which the slab may tear (*Barazangi and Isacks*, 1976, 1979; *Vogt et al.*, 1976); however, its location 150–200 km north of the bend in slab isodepth contours (*Cahill and Isacks*, 1992), coupled with its southward migration from 11°S since it intersected the trench ∼11.2 Ma (*Hampel*, 2002) make such tearing unlikely. Lateral flexure, on the other hand, may be part of the geometrical response of subduction of the Nazca plate beneath the concave shape of the overriding South American plate

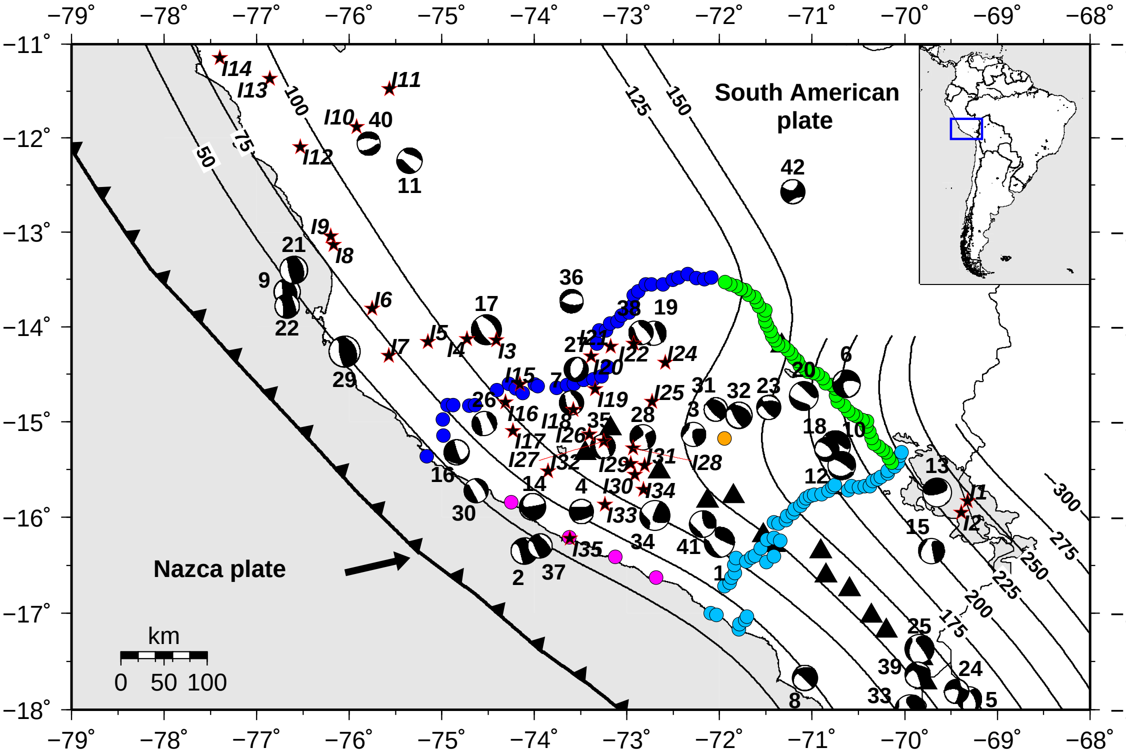

Figure 4.1: Map showing the locations of PeruSE and CAUGHT (orange dots) stations along with events (stars, focal mechanisms) used in this study. The PE (light blue dots), PF (green dots), PG (blue dots), and PH (pink dots) lines of the PeruSE array are shown. Focal mechanisms are from the Global Centroid Moment Tensor (GCMT) catalog (Table 4.1). Events from the International Seismological Centre (ISC) Bulletin event catalog are indicated by italicized labels. The black triangles denote Holocene volcanoes; note the lack of volcanism in the flat slab region. Slab isodepth contours from *Cahill and Isacks* (1992) are shown in thin lines. The convergence direction of the Nazca plate relative to the South American plate near the Peru-Chile Trench is indicated by the black arrow (*DeMets et al.*, 2010). See Figure 4.2 for station names.

(*Bevis and Isacks*, 1984).

A recent deployment of broadband seismometers in southern Peru overlying the transition from flat to normal subduction presents the opportunity to provide further constraints on the nature of this transition as either a smooth contortion or plate tear. Receiver functions along this array suggest a continuous slab with no clear breaks (*Phillips and Clayton*, 2014). In order to test this conclusion and expand on investigations of this region, we use regional earthquakes recorded by the Peru Subduction Experiment (PeruSE) (*PeruSE*, 2013) and Central Andes Uplift and Geodynamics of High Topography (CAUGHT) (*Ward et al.*, 2013) seismic arrays to study the fine-scale structure of the southern Peru subduction zone along the flat-to-normal transition (Figure 4.1). We

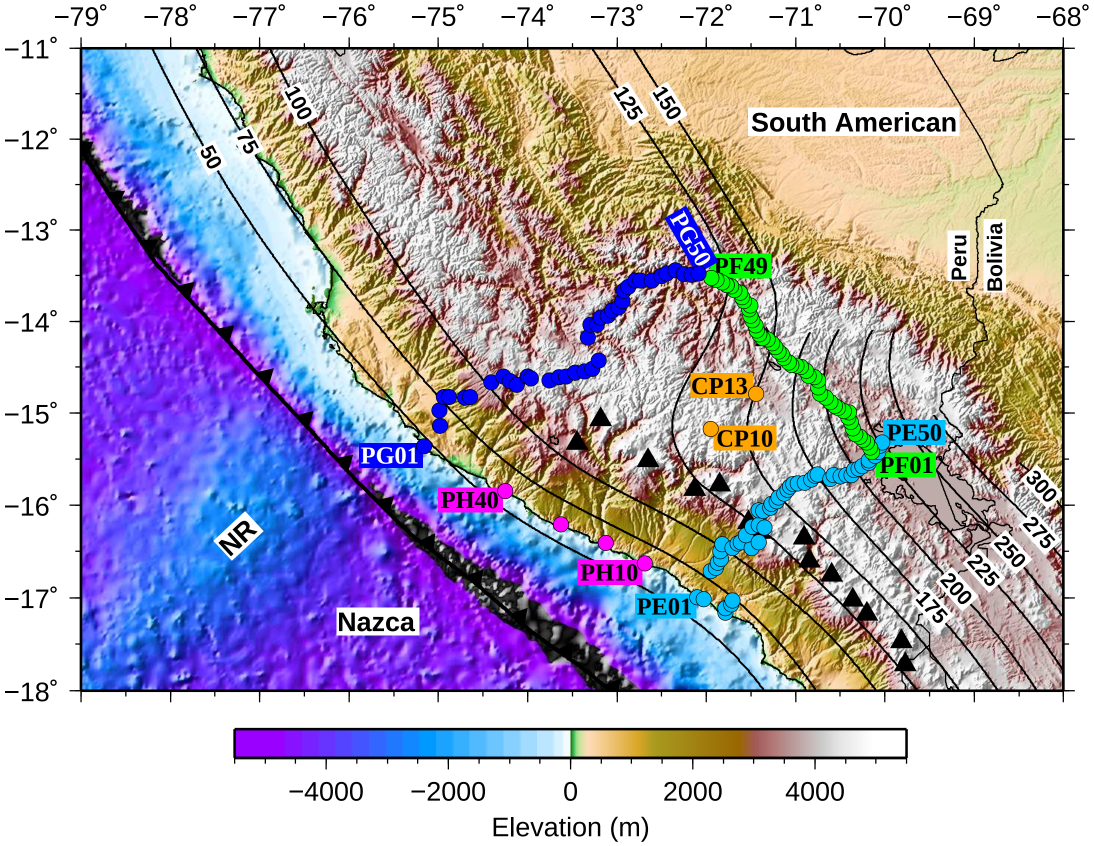

Figure 4.2: Topographic-bathymetric map illustrating the Nazca Ridge (NR) and the high elevation of the Andes. Station and volcano locations are as in Figure 4.1. Stations are numbered sequentially along each line (i.e., PE, PF, PG, and PH) of the PeruSE array with names for endpoint stations indicated. Station names for the two CAUGHT stations (orange dots) are also shown. Topography (*Farr et al.*, 2007) and bathymetry (*Smith and Sandwell*, 1997) data are from the SRTM30_PLUS version 2.0 dataset (http://topex.ucsd.edu/WWW_html/srtm30_plus.html).

analyze seismicity patterns and focal mechanism orientations for any indications of fragmentation or contortion of the subducted plate. We also explore structural features, such as a thin ultra-slow velocity layer (USL) atop the flat slab, that might constrain the slab morphology. Additionally, we perform 2D waveform modeling to image the structure of the subducted Nazca and overriding South American plates in this region, including any potential tears.

4.3 Data Analysis

4.3.1 Data

The seismic data used in this study were recorded by the PeruSE and CAUGHT arrays. The PeruSE array consisted of 100 broadband seismic instruments deployed progressively from July 2008 to February 2013 in four lines (i.e., PE, PF, PG, and PH), comprising a rectangular distribution of 154 stations (Figures 4.1 and 4.2), with each site occupied for ∼2 years. The PE, PF, and PG lines each consisted of 50 stations with an average station spacing of ∼6 km. The PE and PG lines were oriented perpendicular to the trench over the normal and flat subduction regions, respectively. The PF line was oriented parallel to the trench over the downdip flat-to-normal transition. The PH line consisted of 4 stations along the coast. The goal of this experiment was to image the structure of the Peruvian subduction zone in the flat slab, transitional, and normal dipping regions. The CAUGHT array consisted of 50 broadband seismic instruments deployed from November 2010 to August 2012 in a 2D geometry in the Central Andes of northern Bolivia and southern Peru (*Ward et al.*, 2013). Two stations of this array that are located within the interior of the box defined by the PeruSE array (Figure 4.2) are utilized in this study.

We analyze seismograms from 76 regional intraslab earthquakes recorded by these arrays. These events have magnitudes within the range of 4.0 to 6.4 and occur at depths between 46 and 258 km (Table 4.1). The locations of these events are shown in Figure 4.1. Earthquakes whose hypocenters are taken from the International Seismological Centre (ISC) Bulletin event catalog (*International Seismological Centre*, 2011) have identifiers that begin with 'I' (Figure 4.1, Table 4.1). All other events are from the Global Centroid Moment Tensor (GCMT) catalog (*Dziewonski et al.*, 1981; *Ekström et al.*, 2012).

Table 4.1. Events used in southern Peru and their source parameters.

Event ID	Date	Lat (°)	Lon (°)	Depth (km)	Mag	Mechanism Strike/Dip/Rake	Source[a]
1	2008/07/08	-16.26	-72	126	6.2	177/44/-23	1
2	2008/09/20	-16.35	-74.11	52	5.4	303/37/44	1
3	2008/10/15	-15.13	-72.28	134	5	257/58/13	1
4	2008/11/27	-15.94	-73.49	80	5	54/39/52	1
5	2008/12/22	-17.89	-69.3	152	5	333/54/-135	1
6	2009/03/15	-14.6	-70.63	211	5.7	167/63/-25	1
7	2009/06/02	-14.8	-73.6	101	4.9	323/45/-108	1
8	2009/06/13	-17.67	-71.08	95	5.2	237/25/12	1
9	2009/06/15	-13.63	-76.67	52	5.4	330/31/67	1
10	2009/07/12	-15.25	-70.75	197	6.1	101/26/-112	1
11	2009/08/01	-12.24	-75.35	115	5.2	273/48/-135	1
12	2009/09/05	-15.46	-70.68	210	5.8	74/25/-136	1
13	2009/09/30	-15.74	-69.65	258	5.9	315/9/146	1
14	2009/12/24	-15.89	-74.02	71	5.5	165/22/176	1
15	2010/03/22	-16.35	-69.71	218	5.3	235/27/-23	1
16	2010/03/23	-15.32	-74.84	63	5.2	81/22/8	1
17	2010/05/23	-14.03	-74.52	109	6.1	321/37/-97	1
18	2010/06/09	-15.29	-70.84	197	5	78/35/-140	1
19	2010/08/10	-14.07	-72.71	116	5	186/38/-59	1
20	2010/09/13	-14.73	-71.09	171	5.8	93/51/-136	1
21	2010/09/22	-13.4	-76.6	64	5.7	339/30/82	1
22	2010/11/03	-13.78	-76.67	60	5	314/44/40	1
23	2010/11/28	-14.85	-71.47	142	5	256/49/31	1
24	2010/12/15	-17.81	-69.44	157	5.1	8/71/-160	1
25	2011/06/08	-17.37	-69.84	150	5.9	208/32/-27	1
26	2011/07/24	-15.02	-74.54	98	5	308/46/-136	1
27	2011/11/30	-14.45	-73.55	115	5.1	27/46/-72	1
28	2012/01/11	-15.16	-72.83	111	5.2	333/73/-171	1
29	2012/01/30	-14.26	-76.05	46	6.4	323/31/64	1
30	2012/02/12	-15.72	-74.63	81	4.9	316/34/-107	1
31	2012/04/19	-14.87	-72.04	138	4.9	307/30/81	1
32	2012/04/21	-14.93	-71.79	136	5.4	293/36/55	1
33	2012/05/14	-18	-69.94	119	6.3	203/25/-25	1
34	2012/06/07	-15.98	-72.7	120	6.2	110/56/173	1
35	2012/07/13	-15.26	-73.26	117	5.1	175/33/-70	1
36	2012/07/15	-13.73	-73.6	89	4.8	246/33/-119	1
37	2012/09/06	-16.3	-73.94	72	5.1	302/43/54	1
38	2012/09/20	-14.06	-72.85	88	4.9	168/49/-56	1
39	2012/09/29	-17.64	-69.86	146	5.3	252/40/-3	1
40	2012/11/04	-12.06	-75.79	118	4.8	280/48/-59	1
41	2012/11/04	-16.07	-72.18	134	5.5	94/51/-174	1
42	2012/12/30	-12.57	-71.21	51	5	24/71/-9	1
I1	2011/07/14	-15.831	-69.323	233	4.9	—	2
I2	2011/07/14	-15.95	-69.39	236	4.5	—	2
I3	2010/03/19	-14.142	-74.412	104	4.7	—	2
I4	2010/06/26	-14.13	-74.73	94	4.3	—	2

Table 4.1. (continued).

Event ID	Date	Lat (°)	Lon (°)	Depth (km)	Mag	Mechanism Strike/Dip/Rake	Source[a]
I5	2009/01/18	-14.161	-75.15	81	4.7	—	2
I6	2012/05/06	-13.809	-75.752	75	5.1	—	2
I7	2012/03/12	-14.306	-75.573	61	4.7	—	2
I8	2012/01/28	-13.13	-76.17	61	4.1	—	2
I9	2012/06/27	-13.04	-76.2	96	4.4	—	2
I10	2011/09/23	-11.88	-75.923	90	4.5	—	2
I11	2008/12/01	-11.477	-75.569	100	4.7	—	2
I12	2012/05/17	-12.095	-76.526	100	4.4	—	2
I13	2012/12/29	-11.37	-76.86	96	4.6	—	2
I14	2012/12/31	-11.15	-77.401	74	4.9	—	2
I15	2010/08/21	-14.607	-74.156	91	4.1	—	2
I16	2011/07/24	-14.797	-74.31	97	4.9	—	2
I17	2011/05/07	-15.097	-74.233	60	5	—	2
I18	2011/02/17	-14.875	-73.58	98	4.2	—	2
I19	2009/04/25	-14.654	-73.341	87	4.2	—	2
I20	2010/02/28	-14.31	-73.389	83	4.2	—	2
I21	2010/08/11	-14.207	-73.173	86	4.7	—	2
I22	2008/08/06	-14.174	-72.928	94	4.8	—	2
I24	2009/06/20	-14.377	-72.587	86	4.7	—	2
I25	2008/08/20	-14.787	-72.73	99	4.2	—	2
I26	2010/07/11	-15.132	-73.406	103	4.8	—	2
I27	2010/05/30	-15.205	-73.251	104	4.4	—	2
I28	2012/11/30	-15.278	-72.932	103	4.6	—	2
I29	2010/12/27	-15.439	-72.956	102	4	—	2
I30	2008/07/05	-15.557	-72.915	98	4.3	—	2
I31	2012/04/20	-15.46	-72.81	87	4.5	—	2
I32	2008/12/05	-15.519	-73.85	59	4.2	—	2
I33	2011/10/15	-15.866	-73.241	85	4	—	2
I34	2012/02/24	-15.712	-72.821	119	4.7	—	2
I35	2012/02/02	-16.221	-73.615	70	5	—	2

[a] Sources are 1) location, focal mechanism, M_w, and depth from the Global CMT (GCMT) catalog (*Dziewonski et al.*, 1981; *Ekström et al.*, 2012); 2) location, m_b, and depth from the International Seismological Centre (ISC) Bulletin event catalog (*International Seismological Centre*, 2011).

4.3.2 Seismicity

Intraslab seismicity across the study region is examined for any changes, gaps, or patterns that could elucidate the nature of the transition from flat to normal subduction of the Nazca plate. Epicentral locations of 40–300-km-depth earthquakes from the 1960–2013 ISC Bulletin event catalog are shown in Figure 4.3. An abrupt decrease in intermediate depth seismicity can be observed northwest of the PG line of stations, coincident with both the transition to flat subduction and the intersection of

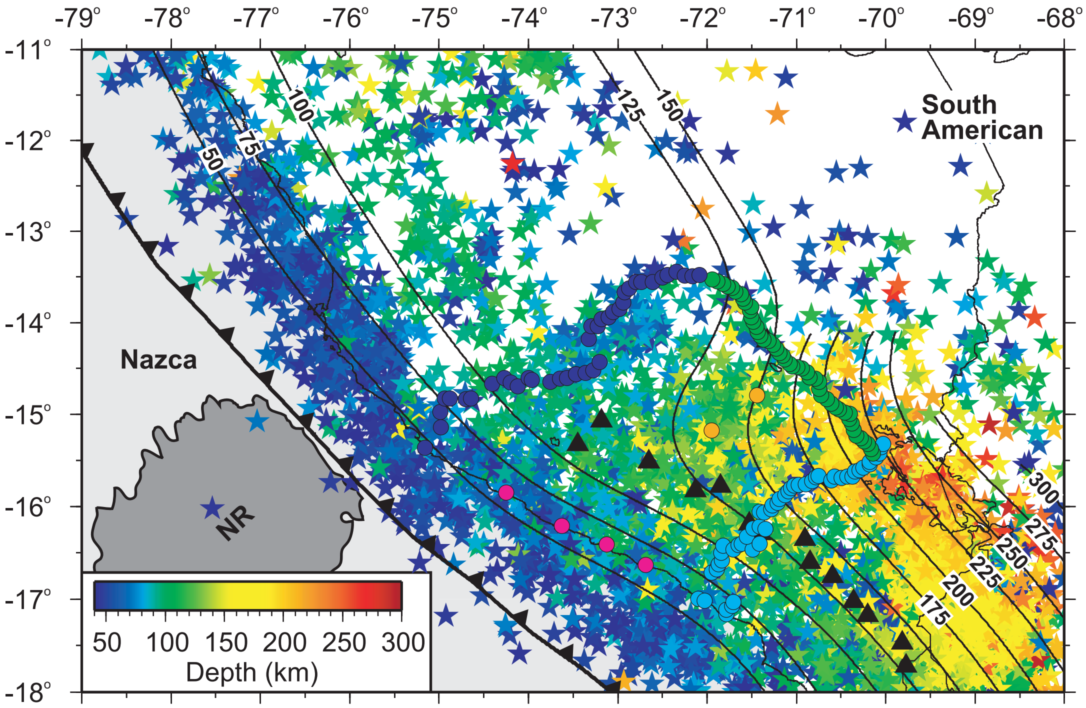

Figure 4.3: Seismicity pattern across the study region. Map of epicenters (stars) for 40–300-km-depth earthquakes from the 1960–2013 International Seismological Centre (ISC) Bulletin event catalog (*International Seismological Centre*, 2011). Epicenters are color-coded by event depth. The dark grey shaded area indicates the Nazca Ridge (NR). Dots are seismic stations (see Figures 4.1 and 4.2). Note the abrupt decrease in intermediate depth seismicity northwest of the PG line of stations, coincident with both the transition from normal (SE) to flat (NW) subduction and the intersection of the NR with the trench. The relative abundance of shallow seismicity within the South American plate overlying the flat slab region should also be noted.

the Nazca Ridge with the Peru-Chile Trench. This decrease in seismicity is indicative of a structural change between the normal dipping region to the southeast and the horizontal slab to the northwest. Additionally, there is a pronounced gap in the intermediate depth seismicity downdip from the Nazca Ridge, which could have implications for the nature of this structural change. This seismicity gap has also been noted by previous authors (*Gutscher et al.*, 1999a; *Hampel*, 2002). The relative abundance of lower crustal seismicity within the South American plate overlying the flat slab region should also be noted for its potential indication of the level of interaction between the two plates. A cluster of seismicity between ∼55 km and ∼85 km depth near the PG line, centered at ∼14°S, 72.85°W (Figure 4.3), may reflect bending of the slab. A cross-section of the seismicity through this cluster is shown in Figure 4.19 of the auxiliary material.

Focal mechanisms of intraslab earthquakes in southern Peru are also analyzed for details of the Nazca slab structure. Source mechanisms of 60–275-km-depth events from the 1976–2013 GCMT catalog are mapped in Figure 4.4. There is a general predominance of normal faulting events below ∼80 km depth, as would be expected for earthquakes which occur in the oceanic lithosphere, as these are typically attributed to bending of the slab and/or slab pull (e.g., *Schneider and Sacks*, 1987; *Suárez et al.*, 1990). The decreased seismicity northwest of the PG line that was noted for the ISC catalog data above is also evident here. Southeast of ∼15.5°S, the events are concentrated in a narrow coast-parallel band between the 100-km and 125-km isodepth contours that only widens near the concave bend in the trench (Figure 4.4) located just south of 18°S (see inset map in Figure 4.1). There is a downdip gap in seismicity between this narrow band and events located northeast of the 175-km isodepth contour. A linear ENE-WSW-oriented concentration of events can also be observed along the sharp bend in isodepth contours through the center of the array, extending continuously from the coast to the 225-km isodepth contour. This concentration of events may have important implications for the morphology of the slab across this region.

The orientations of focal planes across this zone are examined for any information that they can provide about stress within the slab, which could clarify the accommodation mechanism of the flat-to-normal transition. In the horizontal subduction region to the northwest, the normal faulting events primarily exhibit downdip extension. Within the ENE-WSW concentration of events along the change in dip, there are several thrust and oblique faulting events, especially between the 125-km and 150-km isodepth contours (Figure 4.4). The orientations of some of these events show N-S and NW-SE compression. Focal planes for normal faulting mechanisms located near the intersection of the PE and PF lines and slightly to the southeast between the 225-km and 275-km isodepth contours are oriented nearly E-W, indicating NNW-SSE extension. The cluster of shallower seismicity near the PG line noted from the ISC catalog data consists of normal faulting events at various orientations, including those that signify N-S and NW-SE extension. A second cluster of seismicity near the PG line, centered at ∼14.25°S, 73.5°W, is comprised of normal faulting mechanisms showing primarily NW-SE extension.

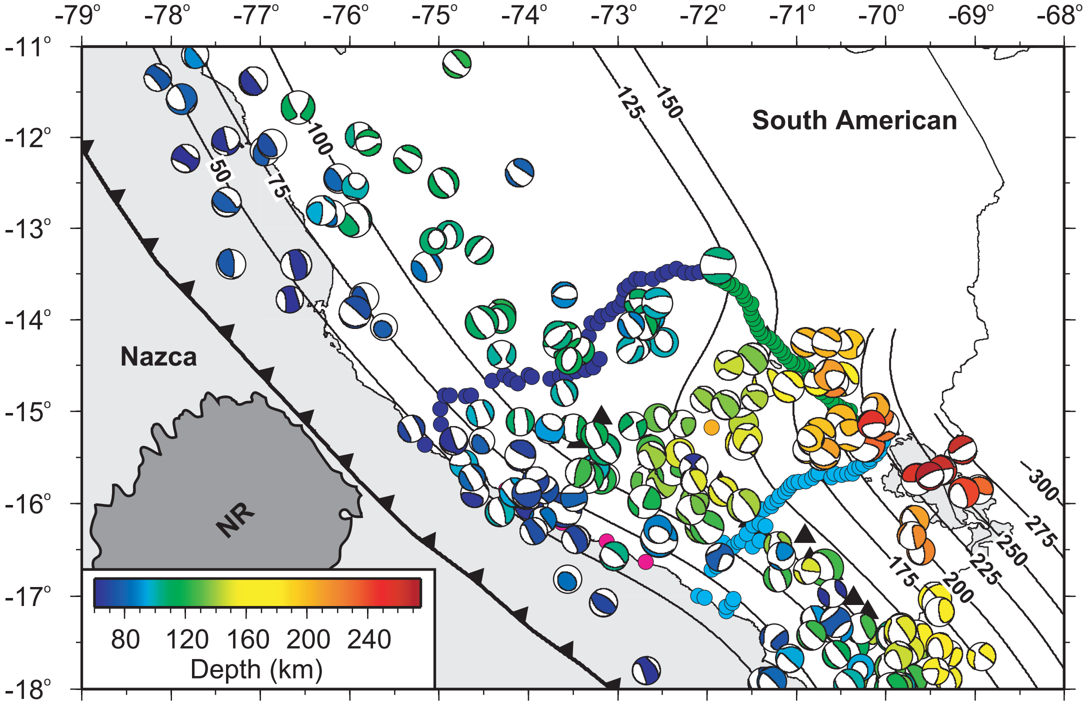

Figure 4.4: Focal mechanisms for intermediate depth earthquakes which occurred in the study region. Map of focal mechanisms from the 1976–2013 Global CMT (GCMT) catalog (*Dziewonski et al.*, 1981; *Ekström et al.*, 2012). Mechanisms are color-coded by event depth and primarily exhibit normal faulting. Note the linear ENE-WSW-oriented concentration of events along the sharp bend in isodepth contours through the center of the array.

4.3.3 Slab Dip

The lateral variation in slab dip across the transition from flat to normal subduction in southern Peru is examined in detail to assess if this change in geometry is accommodated by a smooth contortion of the slab or if there is an abrupt transition which could be indicative of a possible tear. Epicenters for earthquakes from the 1960–2013 ISC Bulletin event catalog are mapped and divided into seventeen 25-km-wide trench-normal bins (Figure 4.5a). Bin 1 overlies the flat slab region across the northwestern extent of the PG line, and bin 17 overlies the normal dipping region along the southeast margin of the PE line. Cross-sections of the seismicity in each bin illustrate variations in the Wadati-Benioff zone across the region and are used to estimate the slab dip in each bin. Examples from bins 5, 13, and 14 are shown in Figure 4.5b-d. Hypocenter locations for earthquakes from the relocated 1960–2008 EHB Bulletin event catalog (*International Seismological Centre*, 2011) are overlain for comparison. There are no systematic differences between the ISC and EHB locations that would affect estimates of slab dip. In general, the ISC data form a scatter envelope around the EHB locations. Thus, the dip angle is estimated by visually selecting ISC hypocenter locations that are downdip of the trench and not within the overriding plate (as defined by teleseismic receiver functions (*Phillips et al.*, 2012; *Phillips and Clayton*, 2014)), then performing a linear regression of the selected locations. The estimated slab dip in bins 5–17 is shown in Figure 4.5e. In order to focus more closely on the transition from flat to normal subduction, results for bins 1–4 are not shown in Figure 4.5e, since, as in bins 5–7, the estimated slab dip in these bins is 0°. The errors on the dip estimates (calculated from the standard deviation in dip) are weighted by the number of earthquakes in each bin, such that fewer events in a bin produces a larger error, with values ranging from ±0.96° (bin 17) to ±3.34° (bin 5). The slab is flat beneath the PG line with its dip gradually increasing in 3° or 5° increments across the transition zone to 19° by bin 13 (Figure 4.5). Between bins 13 and 14, there is the largest incremental increase in slab dip of 8°, followed by an approximately constant dip (27–28°) across the remainder of the bins to the southeast (Figure 4.5).

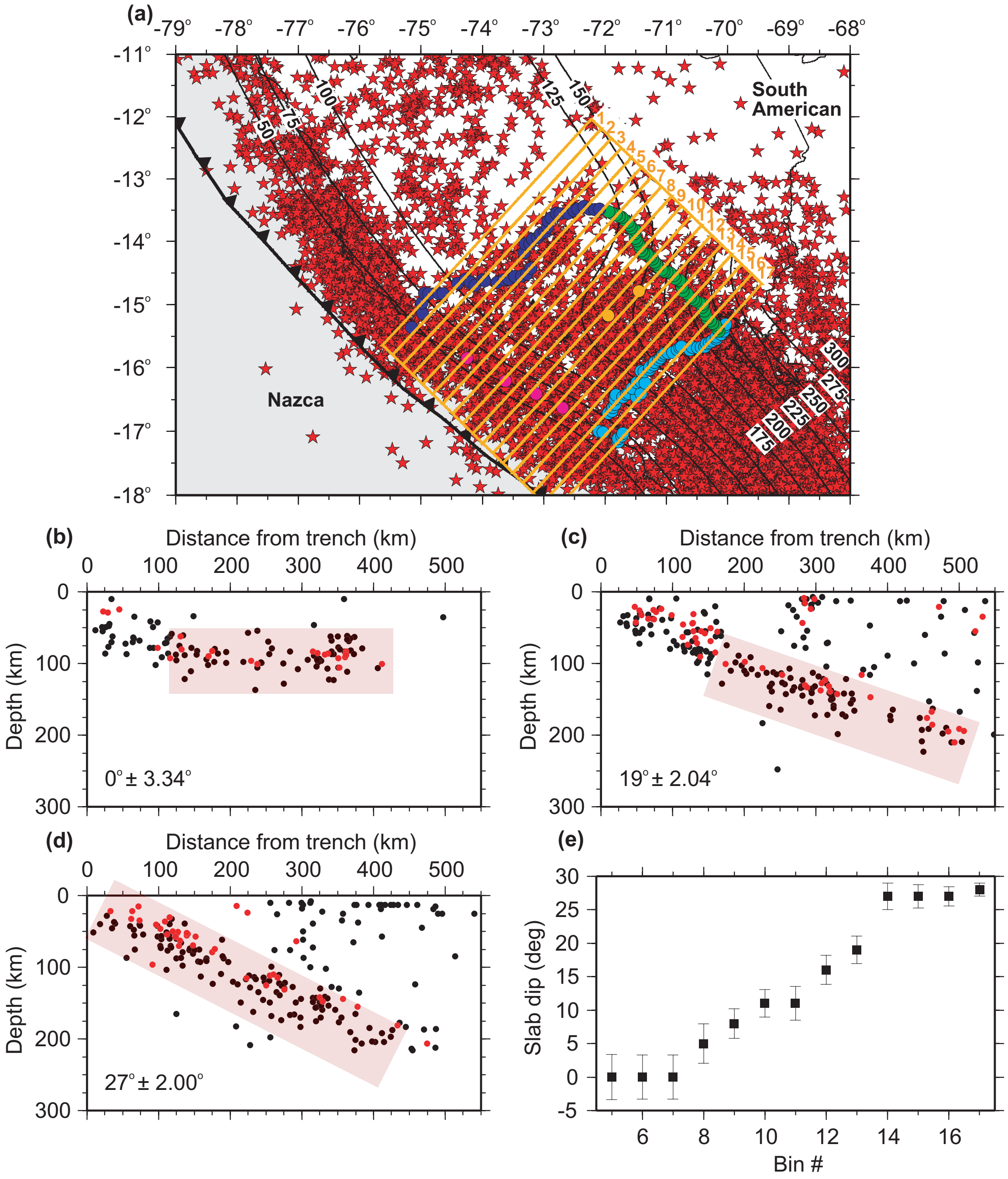

Figure 4.5: Seismicity and slab dip across the transition from flat to normal subduction. (a) Map showing epicenters (stars) for earthquakes from the 1960–2013 ISC Bulletin event catalog (*International Seismological Centre*, 2011). Data in seventeen 25-km-wide bins roughly perpendicular to the trench are analyzed for changes in slab dip across this region. Cross-sections of seismicity (black dots) in bins (b) 5, (c) 13, and (d) 14 are shown along with their respective estimated slab dips. Pink shaded regions reflect the slope of the linear regression and encompass the slab seismicity used to estimate dip. Hypocenter locations for earthquakes from the relocated 1960–2008 EHB Bulletin event catalog (*International Seismological Centre*, 2011) (red dots) are shown for reference. Note the 8° change in slab dip between bins 13 and 14. (e) Plot of slab dip across the data bins. Error bars are weighted by the number of events in each bin, such that fewer events produces a larger error.

4.3.4 Slab Transition

In addition to the along-dip direction, lateral variations in seismicity in the along-strike direction are also analyzed for any gaps or vertical offsets that could indicate plate tearing rather than continuous curvature. Epicenters for earthquakes from the 1960–2013 ISC Bulletin event catalog are mapped and divided into twenty-two 25-km-wide trench-parallel bins that encompass the PeruSE array (Figure 4.6). These trench-parallel (or horizontal) bins are referred to with a preceding 'h' (e.g., bin h1) to distinguish them from the trench-normal bins in Figure 4.5. Bin h1 is located along and just downdip of the trench, while bin h22 is located 50–75 km northeast of the PF line. Note the marked decrease in seismicity in the northwestern portions of bins h19–h22 that expands in lateral extent in the downdip direction. Hypocenter locations from the relocated 1960–2008 EHB Bulletin event catalog are also included in the along-strike seismicity analysis to provide further constraints on the slab location and morphology. For events which can be found in both the ISC and EHB catalogs, only the EHB hypocenter is used. Cross-sections of the ISC and EHB seismicity in each bin illustrate variations in the Wadati-Benioff zone across the region and are used to delineate the transition from flat to normal subduction. Examples from bins h11–h15, located 250–375 km from the trench, are shown in Figure 4.7. No gaps or vertical offsets in the Wadati-Benioff zone seismicity can be observed in the cross-sections. Rather, a continuous transition from horizontal to 28° dipping slab is observed.

A weighted least-squares piecewise-linear regression fit to the slab seismicity in each cross-section is performed using the Shape Language Modeling toolkit (*D'Errico*, 2009) in order to approximate the slab morphology across the transition. Events located within the overriding plate and any deep outliers (determined visually) are weighted to 0. Individual ISC hypocenters offset from the main concentration of slab seismicity and/or from the overall slab trend approximated from the EHB hypocenters are weighted to 0.25–0.75, depending on the degree of offset, with the largest offset events weighted the lowest. All other events are weighted to 1. The fits for bins h11–h15 are shown in Figure 4.7. Due to the marked decrease in seismicity in the northwestern portions of bins h19–h22, there is insufficient data to perform piecewise-linear regression fits in these bins. The complete

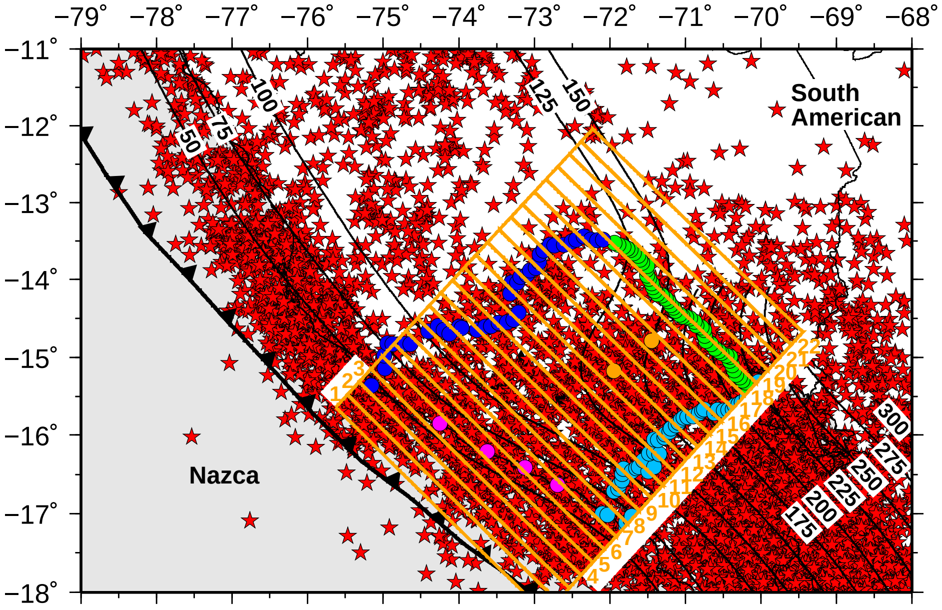

Figure 4.6: Map showing epicenters (stars) for earthquakes from the 1960–2013 ISC Bulletin event catalog as in Figure 4.5a. Data in twenty-two 25-km-wide bins roughly parallel to the trench are used to constrain the transition from flat to normal subduction across this region. These trench-parallel (or horizontal) bins are referred to with a preceding 'h' to distinguish them from the trench-normal bins in Figure 4.5. Note the marked decrease in seismicity in the northwestern portions of bins h19–h22.

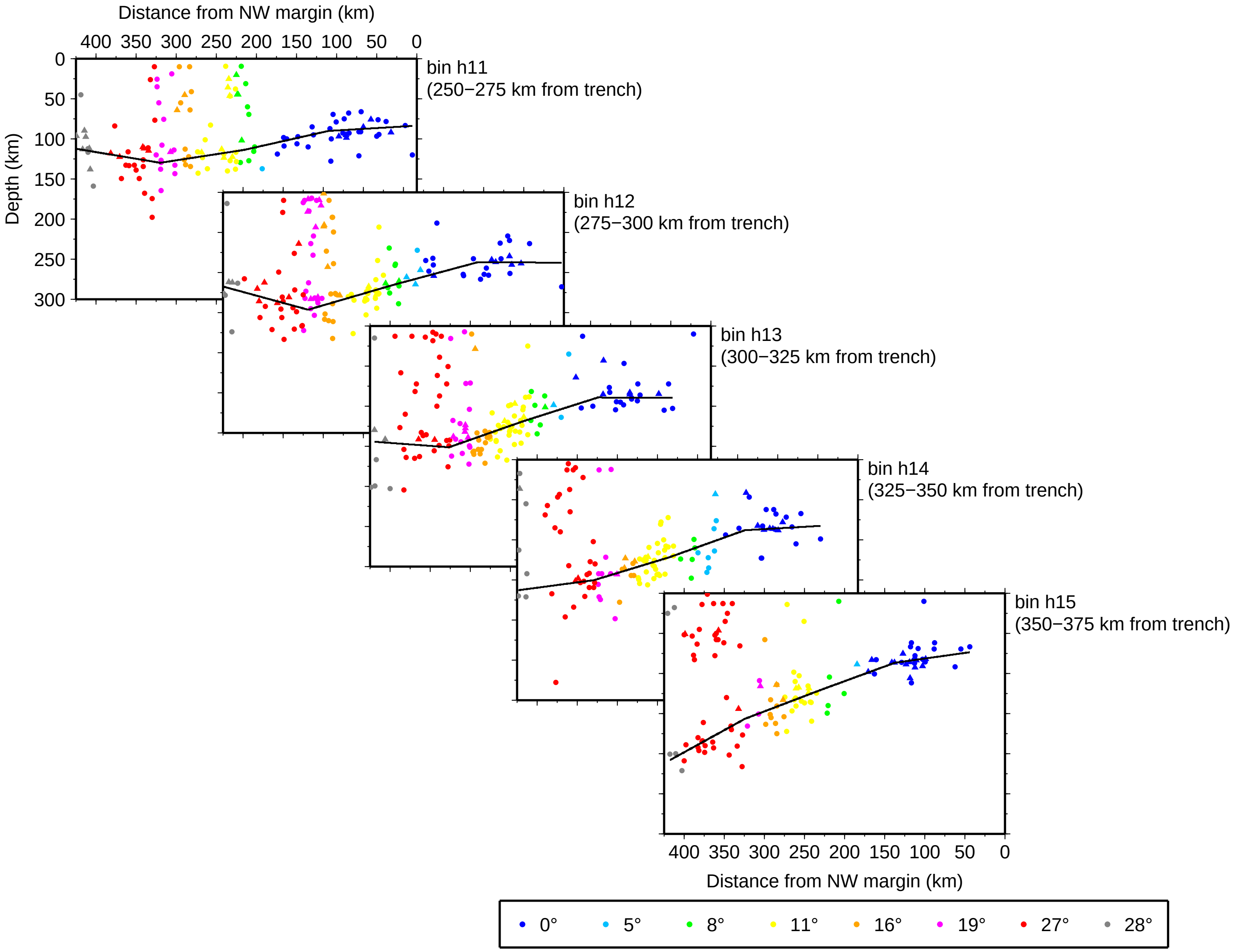

Figure 4.7: Cross-sections of seismicity from the ISC (dots) and EHB (triangles) catalogs in trench-parallel bins h11–h15 (see Figure 4.6 for bin locations). Hypocenter locations are colored to reflect slab dip as estimated in Figure 4.5. Weighted piecewise-linear regression fits to the slab seismicity in each cross-section are shown (black lines). Note the smooth transition from horizontal to 28° dipping slab without any gaps or vertical offsets in the seismicity. See Figure 4.20 of the auxiliary material for the complete set of seismicity cross-sections (bins h1–h18).

set of seismicity cross-sections (i.e., bins h1–h18), including fits, can be found in Figure 4.20 of the auxiliary material. Consistent with the lack of gaps and vertical offsets observed in the seismicity, the fits in each cross-section do not show any sharp changes in the slab shape. The fit for bin h17 is an exception to this, where an abrupt step can be observed due to a poorly constrained regression from sparse data in this bin (Figure 4.20). As such, bin h17 is excluded from further analyses.

The weighted piecewise-linear regression fits to the slab seismicity in trench-parallel cross-sections h1–h18 (with h17 removed; Figure 4.8a) are used to estimate a 3D slab surface in an attempt to image the flat-to-normal transition. The gridfit function of *D'Errico* (2005) is used to approximate the slab surface on a 425-km-by-450-km grid that extends to ∼210 km depth from the seventeen seismicity fits. Each fit is placed at the midpoint of its 25-km-wide bin for determining its distance from the trench in the grid. For example, bin h1 encompasses 0–25 km from the trench, so its fit is placed at 12.5 km from the trench. The resultant 3D slab surface is shown in Figure 4.8b. Observed vertical oscillations, or waviness, of the slab surface are likely artificial and are the result of 25-km-wide gaps between the location of each seismicity fit. An increase in the smoothing parameter applied to the surface estimate by two orders of magnitude significantly reduces the amplitude of the waviness of the surface; however, it also results in a shallowing that is inconsistent with the seismicity. As such, the slab surface as shown in Figure 4.8b, with very little smoothing applied, is a more accurate representation of the data. The addition of interpolated lines located at the midpoints between each seismicity fit, effectively reducing the 25-km-wide gaps to 12.5-km-wide gaps, increases the frequency of the waviness of the surface, further supporting the relative accuracy of the slab surface as shown in Figure 4.8b. An anomalous rise in the northwestern corner (∼0–150 km from the NW margin) of the slab surface in the downdip region (∼325–450 km from the trench) should also be noted. Possible implications of this feature will be discussed in section 4.4.

4.3.5 Ultra-slow Velocity Layer

Investigation of a fine-scale structural feature, such as an USL, can provide further information on the nature of the transition from flat to normal subduction. The existence of such a layer is searched

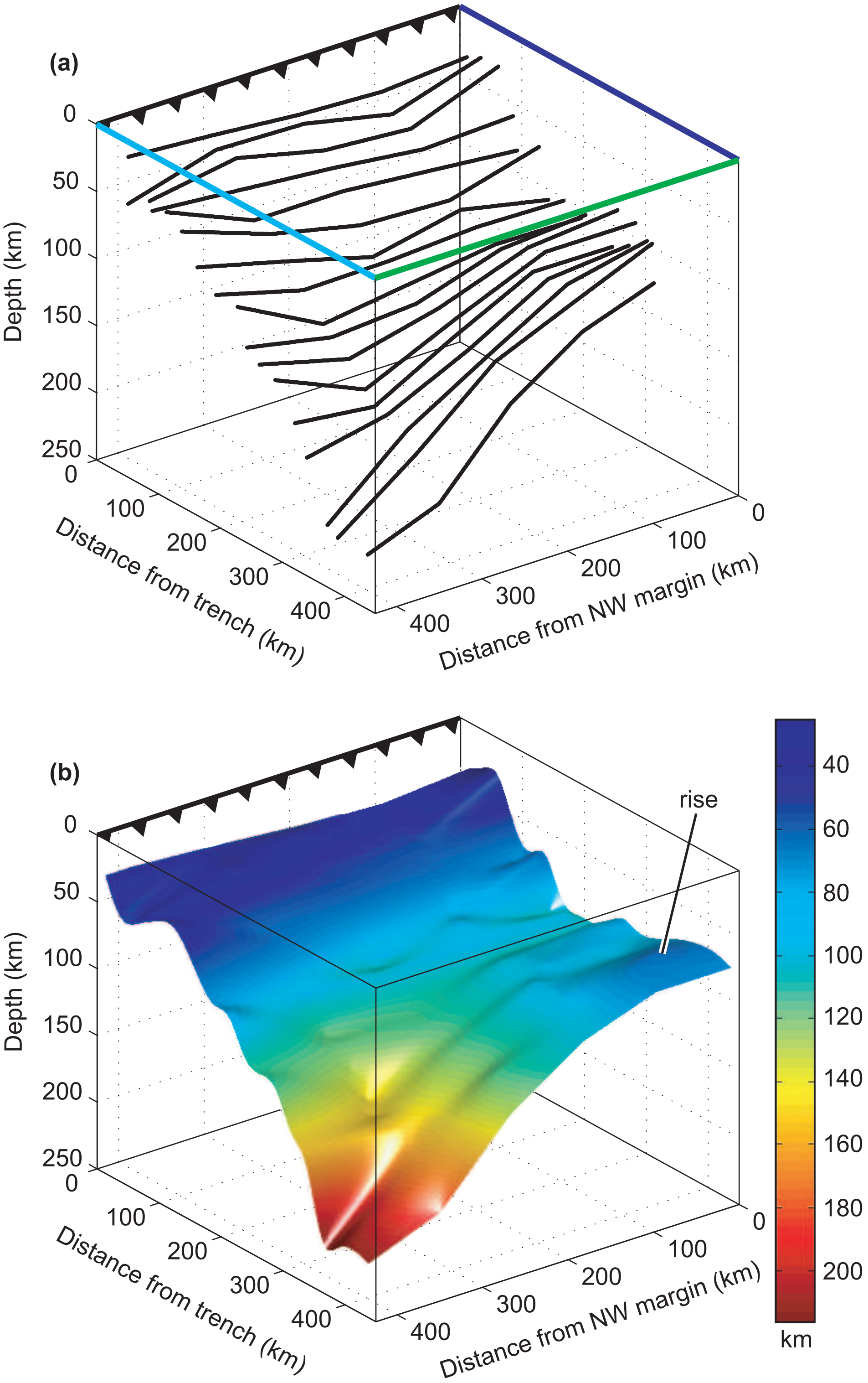

Figure 4.8: 3D perspective view (looking west) of the transition from flat to normal subduction as constrained by seismicity. (a) Weighted piecewise-linear regression fits to the slab seismicity in trench-parallel cross-sections h1–h18 shown in 3D. The fit for bin h17 is excluded due to a poorly constrained regression from sparse data in this bin (see Figure 4.20 of the auxiliary material). At the surface, the boundaries of the box are colored to reflect their correspondence with the approximate locations of the PG (blue), PF (green), and PE (light blue) lines of the PeruSE array (Figure 4.6). (b) 3D slab surface generated from seismicity fits in (a). Note the anomalous rise in the northwestern corner of the slab surface in the downdip region, which may be due to decreased seismicity in this region (Figure 4.6). Trench location is indicated by barbed line.

for in southern Peru, with potentially important implications for slab tearing if its lateral extent is coincident with other possible tear indicators. The USL as explored here was first imaged atop the flat Cocos slab in central Mexico as a 3–5-km-thick layer at a depth of 45–50 km with a V_P of 5.4–6.2 km/s and a V_S of 2.0–3.4 km/s (*Song et al.*, 2009; *Kim et al.*, 2010). Its anomalously low shear wave velocity suggests a relationship with fluids, specifically free water or hydrous minerals, in the subduction zone; however, the exact nature of the USL is not known. *Song et al.* (2009) proposed that the USL represents a fluid-saturated portion of the oceanic crust, forming a high pore fluid pressure (HPFP) layer that is sealed by some low permeability layer, such as fine-grained blueschist, directly above it. Thermal modeling of the central Mexico subduction zone found a high pore pressure ratio of 0.98 along the subduction interface (*Manea et al.*, 2004), consistent with *Song et al.* (2009)'s HPFP layer. *Kim et al.* (2010), on the other hand, proposed that the USL is highly heterogeneous upper crust that is composed of mechanically weak hydrous minerals (talc) that might be under high pore pressure. With or without free fluid, *Kim et al.* (2013) demonstrate that a talc-rich ultramafic layer is required to explain the observed USL velocities and suggest that this talc originates from the mantle wedge during the slab flattening process. Similarly, *Manea et al.* (2013) propose that the USL represents a remnant of mantle wedge that experienced significant serpentinization since the slab flattened. The hydrous minerals and/or high pore pressure of the USL characterize it as a low strength layer, which may be responsible for the flat subduction geometry (*Manea and Gurnis*, 2007; *Kim et al.*, 2010) and the observed decoupling of the flat Cocos slab from the overriding North American plate (*Singh and Pardo*, 1993; *Franco et al.*, 2005) in central Mexico.

The presence of the USL atop the Nazca slab is identified by the existence of complex P waveforms (*Song et al.*, 2009) recorded by the PeruSE and CAUGHT arrays. As described by *Dougherty et al.* (2012) for the case of the Cocos slab, these complex P waveforms consist of three locally converted S-to-P phases (A, B, C) that arrive within 4 sec after the P-wave (Figure 4.9). Phase A converts at the bottom of the USL and appears as a negative pulse at local stations. Phase B arrives immediately after phase A as a positive pulse, indicative of an S-to-P wave that converted at the top of the USL. Phase C converts at the base of the high velocity layer, arriving before phase A and ∼1.0–1.5 sec after the direct P-wave (*Song and Kim*, 2012). These three phases are searched for in the seismograms of the intraslab earthquakes analyzed in this study. P waveforms in these seismograms are categorized as complex, possibly complex, or simple based on the existence or absence and nature of phases A, B, and C. Examples of these waveforms from event 17 recorded at PeruSE stations are shown in Figure 4.9. The waveforms have been bandpass filtered to 0.01–0.6 Hz, with the shorter periods in the frequency band allowing for the identification of the three S-to-P phases. When all three of the phases are readily observed, the waveform is deemed complex. If one of the phases is not easily identified due to an uncharacteristic pulse shape and/or amplitude, but the other two phases are clearly visible, then the waveform is possibly complex. Simple waveforms lack the shoulder in the direct P pulse representative of the C phase and also have uncharacteristically shaped and/or low amplitude A and B phases, indicating that there is no HVL or USL present, respectively. The arrival times of the possible A and B phases in the simple waveforms are also inconsistent with the presence of the USL (i.e., they arrive too early).

The lateral extent of the USL in southern Peru is mapped by examining the status of the layer at each epicentral event location (Figure 4.10). We identify seven events which indicate the presence of the USL from their P waveforms. Another 14 events possibly indicate the presence of the USL. The presence of the USL is undetermined for three events due to low signal-to-noise ratio, and the remaining 52 events in our dataset indicate that no USL is present at their locations. In general, the events which suggest (or possibly suggest) the existence of the USL are concentrated in the flat slab region along and northwest of the PG line, while those that suggest the USL is lacking are concentrated to the southeast, where the slab dip is increasing and normal subduction occurs. There is no overlap between the USL or possible USL locations and the no USL events. It should also be noted that the events which indicate the presence of the USL are all located directly downdip from the Nazca Ridge where it intersects the trench. The projected linear continuation of the Nazca Ridge is indicated in Figure 4.10. The width of this linear extension is constrained by the current width of the ridge near the trench (Figure 4.10). Previous authors have identified the Tuamotu Plateau on the Pacific plate as the conjugate feature to the Nazca Ridge (e.g., *Pilger*, 1981; *Pilger*

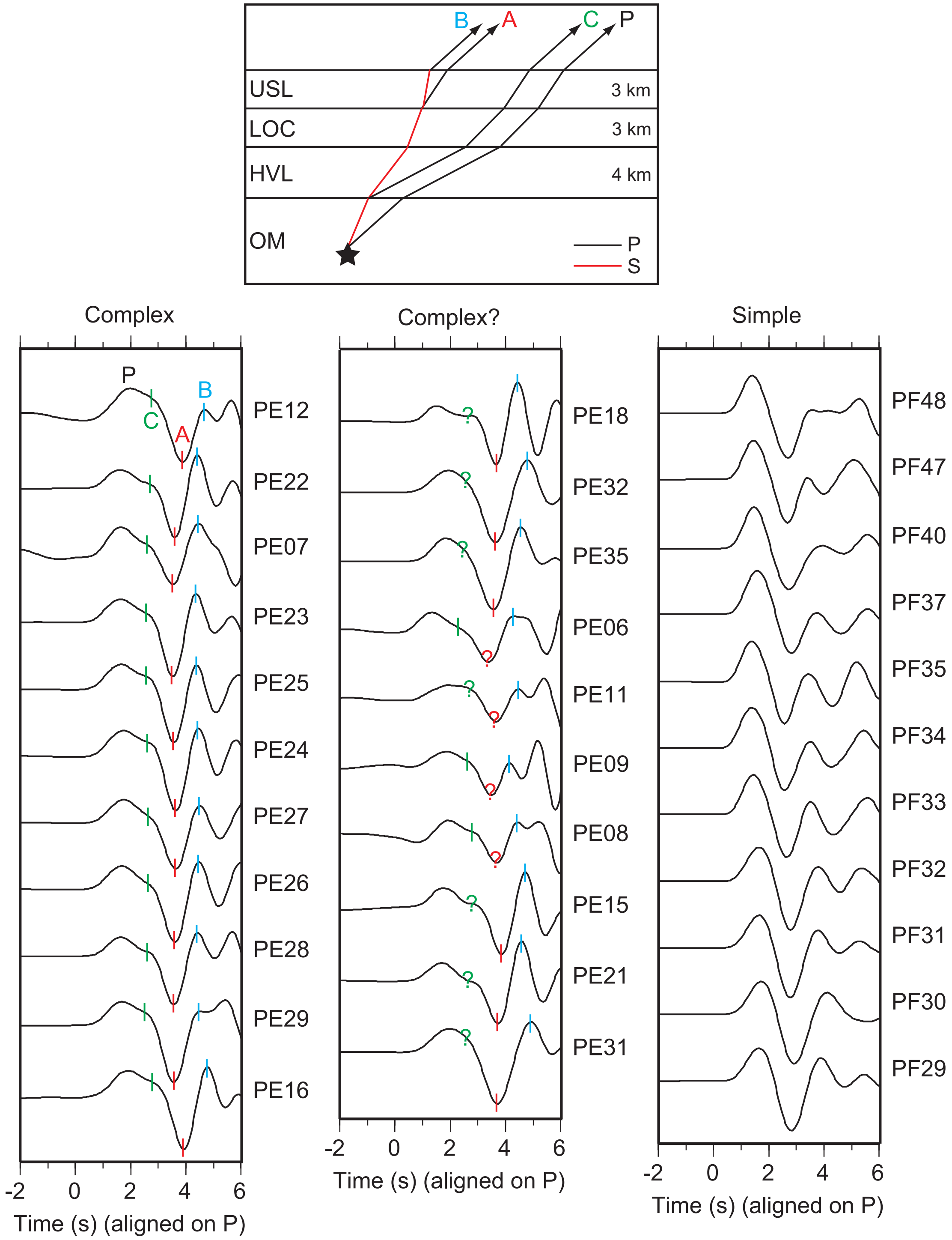

Figure 4.9: (top) Schematic cross-section illustrating the raypaths of the P-wave and the three S-to-P phases (A, B, C) that comprise the complex P waveform. Abbreviations are USL, ultra-slow velocity layer; LOC, lower oceanic crust; HVL, high velocity layer; OM, oceanic mantle. Approximate layer thicknesses for the USL, LOC, and HVL are indicated. (bottom) Examples of (left) complex, (middle) possibly complex, and (right) simple P waveforms from event 17 recorded on the vertical component by PeruSE stations and filtered to 0.01–0.6 Hz. S-to-P phases A, B, and C are indicated by red, blue, and green tick marks, respectively. All three of these phases are visible in the complex waveforms within 4 sec of the P-wave. Question marks on the possibly complex waveforms indicate a phase that is not easily identified due to an uncharacteristic pulse shape and/or amplitude. Simple waveforms lack the shoulder in the direct P pulse indicative of the C phase and also have uncharacteristically shaped and/or low amplitude A and B phases, indicating there is no HVL or USL present, respectively. Modified from *Dougherty et al.* (2012).

and Handschumacher, 1981; *Woods and Okal*, 1994) and used its size and location to approximate the downdip continuation of the Nazca Ridge beneath South America (e.g., *Pilger*, 1981; *von Huene et al.*, 1996; *Gutscher et al.*, 1999a; *Hampel*, 2002). A recent geochronological and geochemical study of lavas from the Nazca Ridge, however, indicated that the ridge formed at a hotspot located well to the east (i.e., at least 500 km) of the Pacific-Farallon spreading center (*Ray et al.*, 2012), and, as such, the Tuamotu Plateau cannot be its conjugate feature. Note the coincidence of the approximate boundary between the USL or possible USL locations and the no USL locations with the southeast margin of the projected continuation of the Nazca Ridge. Shaded contours of the USL, possible USL, and no USL zones further clarify our observations (Figure 4.10).

The locations of the S-to-P conversion points from the top of the Nazca slab are also mapped in order to illustrate where the slab is sampled to produce complex, possibly complex, and simple P waveforms (Figure 4.11). These S-to-P conversion point locations are approximated as 10% of the distance from the source to the receiver along a direct path. Conversion point locations for simple P waveforms indicate where no USL is present (Figure 4.11a), while those for possibly complex waveforms indicate where the USL is possibly present (USL?; Figure 4.11b). The complex P waveform conversion point locations denote where the USL is present (Figure 4.11c). The intermingling of S-to-P conversion points indicative of the USL or possible USL with those that signify no USL northwest of the PG line in the flat slab region suggests that the USL is likely laterally heterogeneous, consistent with previous observations in central Mexico (*Song et al.*, 2009; *Kim et al.*, 2010; *Dougherty et al.*, 2012). Other observations of patterns in USL, possible USL, and no USL locations, as noted for Figure 4.10 above, also apply here.

4.3.6 2D Velocity Modeling

The shallow seismic structure of the southern Peru subduction zone is examined in 2D using a finite-difference wave propagation algorithm with GCMT focal mechanisms (Table 4.1). The P- and S-wave velocities from three different models (Figure 4.12) are coupled with subducted slab geometries estimated from two different sets of isodepth contours (Figure 4.13) in an effort to constrain the

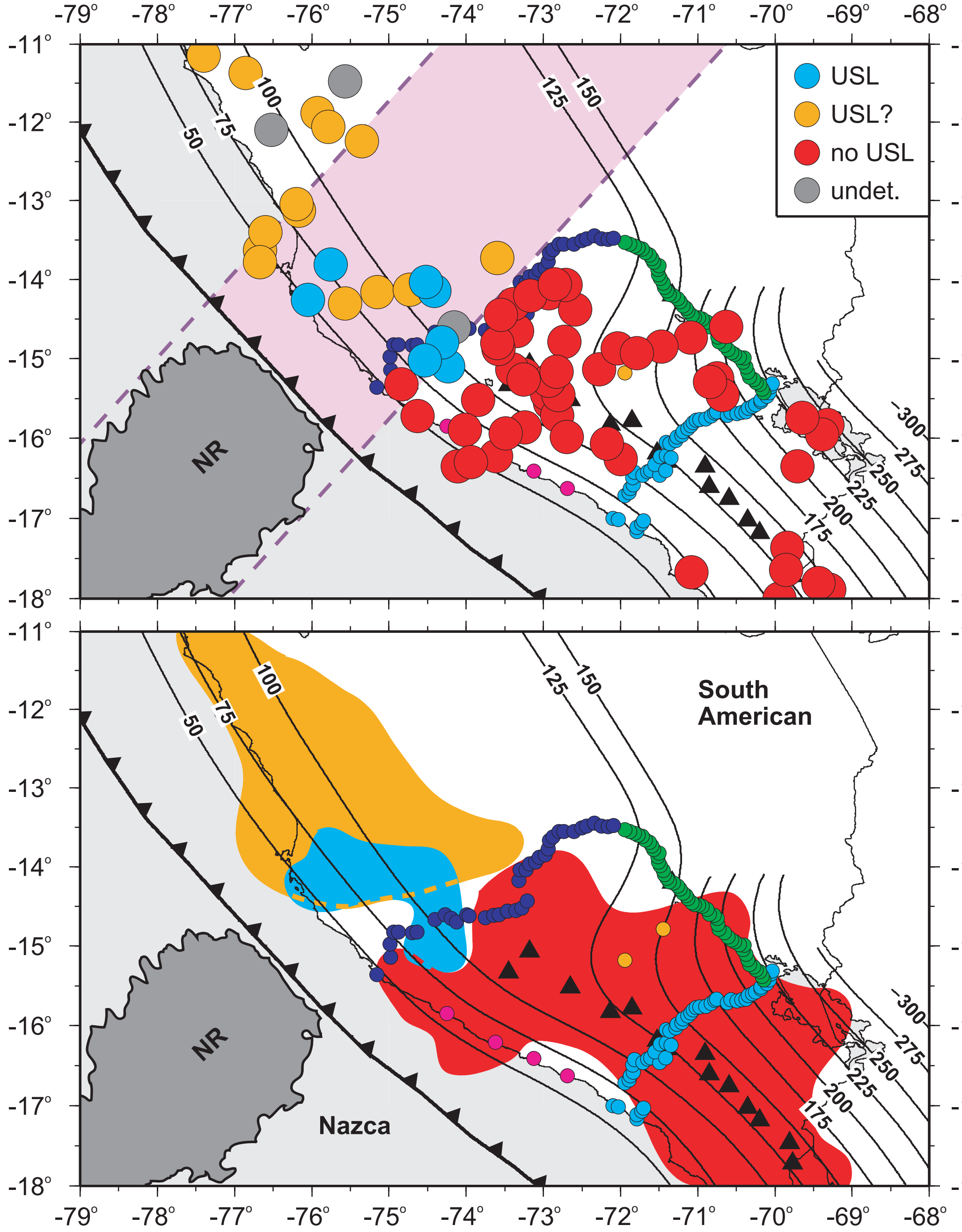

Figure 4.10: Mapping the lateral extent of the USL using PeruSE P waveforms. (top) Events which indicate the presence of the USL are shown in blue. Those which possibly indicate the USL is present are shown in orange. Red events indicate no USL is present. The presence of the USL is undetermined for grey events. The projected linear continuation of the NR is indicated by the purple shaded region. Note the transition from USL and possible USL events to no USL events along the SE margin of this feature. (bottom) Shaded contours of USL, possible USL, and no USL zones.

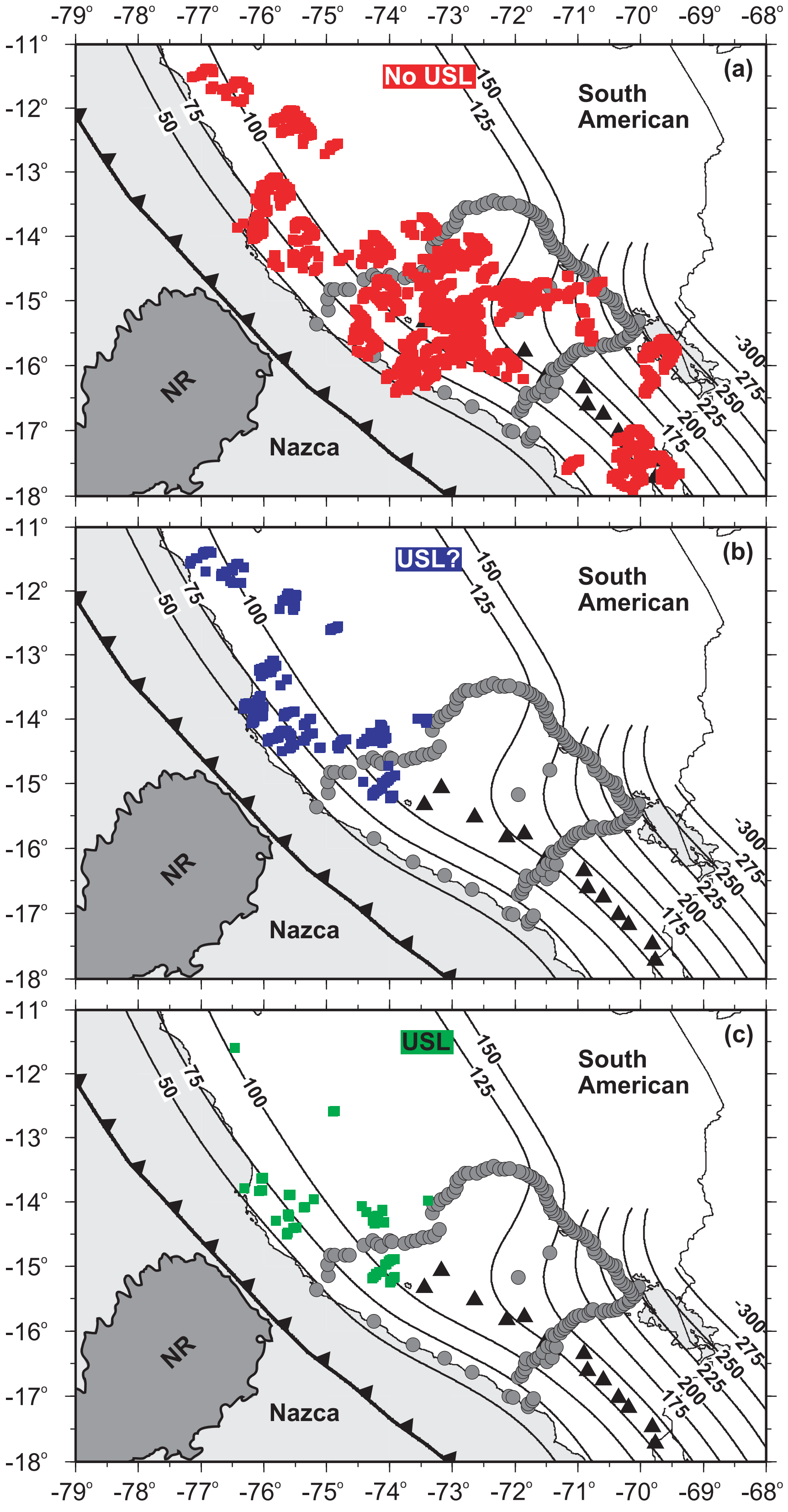

Figure 4.11: Approximate locations of S-to-P conversion points from the top of the Nazca slab for waveforms recorded at PeruSE stations. Conversion points for waveforms which indicated (a) no USL is present, (b) possible USL presence, and (c) USL is present are shown. Compare the locations of these conversion points to the zones in Figure 4.10.

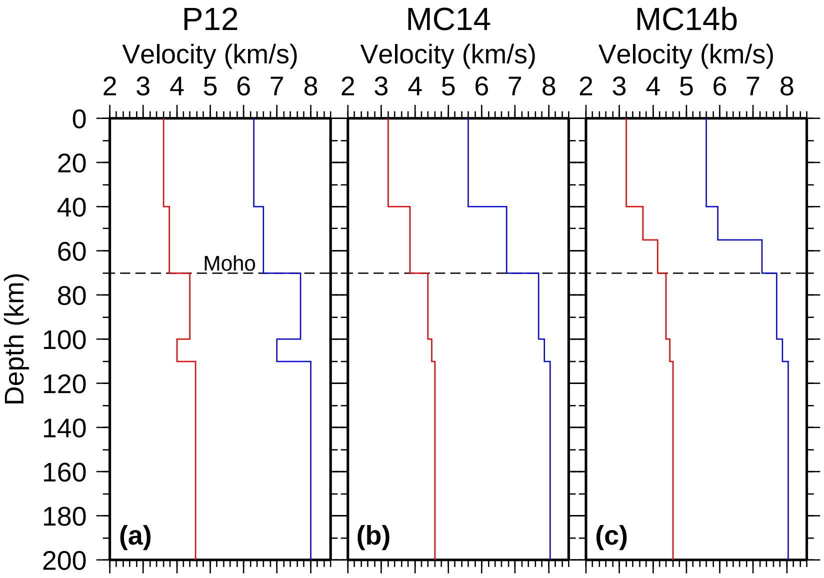

Figure 4.12: 1D P (blue) and S (red) wave velocity models tested in this study. (a) Southern Peru velocity model from receiver function study by *Phillips et al.* (2012) (P12). The Moho depth is indicated by the black dashed line. (b) Simplified southern Peru velocity model from surface wave study by *Ma and Clayton* (2014) (MC14). (c) Variation on MC14 velocity model with lower crust of the overriding plate subdivided into two layers (MC14b).

structure and morphology of the Nazca slab. The three velocity models tested are: (1) southern Peru velocity model from receiver function study by *Phillips et al.* (2012) (P12) (Figure 4.12a); (2) simplified southern Peru velocity model from surface wave study by *Ma and Clayton* (2014) (MC14) (Figure 4.12b); (3) variation on MC14 velocity model with the lower crust of the overriding plate subdivided into two layers (MC14b) (Figure 4.12c). *Phillips et al.* (2012)'s receiver function results are used to constrain the depths of the crustal and mantle discontinuities in the MC14 and MC14b models. A simplified 1D average of S-wave velocities from 2D cross-sections in *Ma and Clayton* (2014) is used to generate the MC14 and MC14b models. The corresponding P-wave velocities are calculated using an average V_P/V_S ratio of 1.75 (*Phillips and Clayton*, 2014). These models exclude the low velocity zone imaged in portions of the overriding plate (*Ma and Clayton*, 2014) for simplicity. Additionally, the well-established isodepth contours of *Cahill and Isacks* (1992) are tested in comparison to the more recent contours of Slab1.0 (*Hayes et al.*, 2012) in order to ascertain which might be a better representation of the actual slab geometry. Both sets of contours are derived from hypocenter locations.

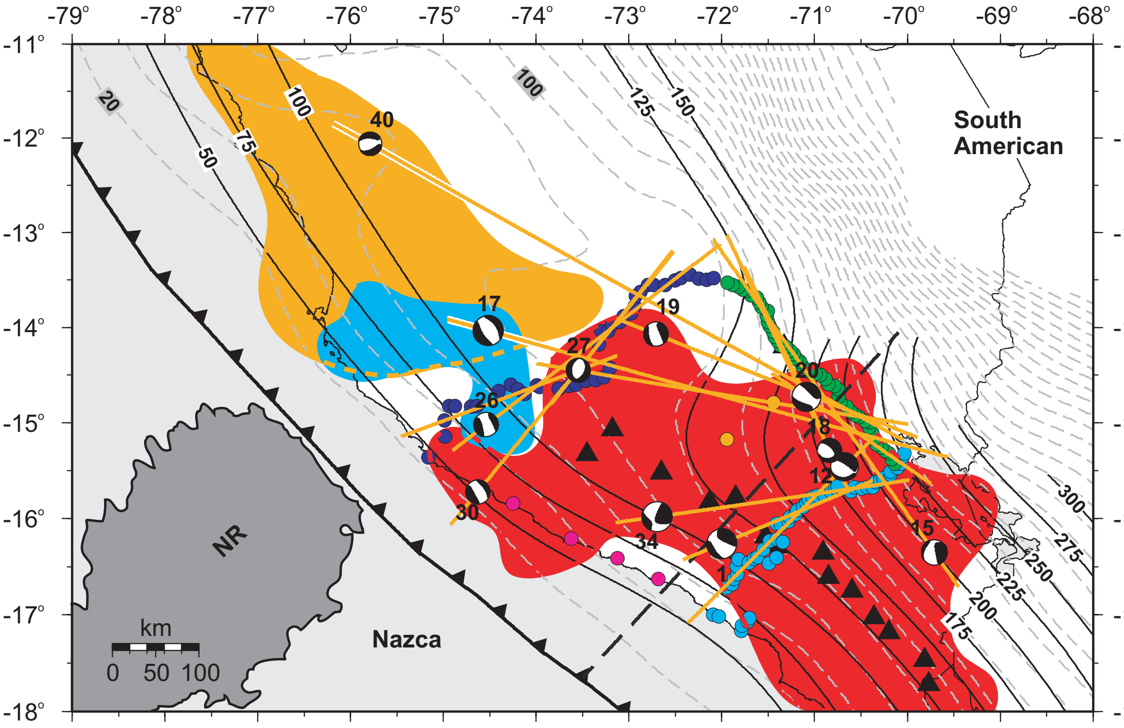

Figure 4.13: Map of locations of 2D velocity model cross-sections (orange lines) for the twelve events modeled (focal mechanisms). The USL (blue), possibly USL (orange), and no USL (red) zones from Figure 4.10 are shown. The boundary between bins 13 and 14 of Figure 4.5, demarking the largest change in slab dip (8°), is denoted by the black dashed line. Slab isodepth contours from Slab1.0 (*Hayes et al.*, 2012) are shown in grey dashed lines. The 20-km and 100-km contours are labeled for reference. Model parameters and results for each 2D profile can be found in Table 4.2.

We generate synthetic seismograms for particular 2D velocity and slab geometry models and compare them to the data for 12 events. These models are oriented along 15 different profiles throughout the study region, concentrated across the transition between flat and normal subduction in order to examine the nature of this change in slab dip (Figure 4.13, Table 4.2). Note that for event 20 both a N26°W-oriented profile and a S56°E profile are modeled. Three different profiles (i.e., N39°E, S81°E, and S70°W) are also modeled for event 27. For each 2D model, we test for the presence of any of four possible slab structural features that may exist along the profile, depending on its location. These features include a 3-km-thick USL (V_S of 2.6 km/s) at the top of the slab, the projected downdip extension of the Nazca Ridge, a tear in the slab located along the southeast margin of the projected Nazca Ridge, and a tear in the slab located along the largest transition (i.e., 8°) in dip (Figure 4.13, Table 4.2). The USL is limited to only those regions encompassed by the USL and possible USL zones as defined in Figure 4.10. The projected continuation of the Nazca Ridge is modeled to be only as wide as its current expression near the trench (∼250 km) and 18 km thick across its center (*Couch and Whitsett*, 1981; *Woods and Okal*, 1994). Each of the two possible slab tears are modeled as 20-km and 50-km-wide gaps in the plate, centered at their respective feature of interest (i.e., ridge margin or change in dip).

The 2D modeling results for all of the events tested are summarized in Table 4.2, with the best-fitting velocities and slab geometry for each profile indicated, along with the status (i.e., confirmed presence, not present, or inconclusive) of any structural features tested. In general, the P12 velocity model produces synthetics that are better representations of the observed data than the MC14 or MC14b models, although there is some discrepancy between the vertical and radial components along four profiles in which the MC14 model provides a better fit to the radial component data than the P12 model. The MC14 model only provides the best fit to the data on both vertical and radial components for events 17 and 40. Similarly, the MC14b model is the best-fitting model only for the S81°E profile of event 27. All three of these events are located in same general area of our study region, along and northwest of the PG line, and their respective profiles are oriented within a ∼20° azimuth window (Figure 4.13, Table 4.2). However, the data from a nearby event (i.e.,

Table 4.2: Model parameters and results for each 2D profile in southern Peru.

Event ID	Profile azimuth (°)	Profile length (km)	1D Velocity model[a]	Slab geometry[b]	Feature(s) tested[c]	Results[d]
1	N68E	245	P12(Z), MC14(R)	S1	n/a	—
12	S46W	300	P12	S1	n/a	—
15	N36W	480	P12(Z), MC14(R)	S1	dip tear	No tear
17	S73E	600	MC14	S1	USL, ridge, ridge tear, dip tear	USL: inconclusive, ridge: confirmed, no tears
18	N26W	330	P12	CI	dip tear	No tear
19	S68E	385	P12	CI	dip tear	No tear
20	N26W	220	P12	S1	n/a	—
	S56E	230	P12(Z), MC14(R)	S1	dip tear	No tear
26	N53E	390	P12	S1	USL	Possibly confirmed
27	N39E	230	P12	S1	n/a	—
	S81E	450	MC14b	S1	dip tear	No tear
	S70W	275	P12	S1	USL	Confirmed
30	N40E	415	P12	CI	USL	No USL
34	N82E	355	P12(Z), MC14(R)	S1	dip tear	No tear
40	S60E	750	MC14	CI	USL, ridge, ridge tear, dip tear	USL: confirmed, ridge: inconclusive, no tears

[a] Best fitting 1D velocity model when applied in 2D. P12 is from *Phillips et al.* (2012); MC14 and MC14b are from *Ma and Clayton* (2014). Variable results between vertical (Z) and radial (R) components are indicated.

[b] Slab geometry which most accurately predicts the observed waveforms when coupled with the best fitting 1D velocity model(s). Possible geometries are estimated from the slab isodepth contours of *Cahill and Isacks* (1992) (CI) and Slab1.0 (*Hayes et al.*, 2012) (S1).

[c] Slab structural feature(s) tested along each profile, which include: an ultra-slow velocity layer at the top of the slab (USL), the projected downdip extension of the Nazca Ridge (ridge), a tear in the slab located along the SE margin of the projected Nazca Ridge (ridge tear), and a tear in the slab located along the sharpest transition in dip (dip tear).

[d] Modeling results for each slab feature tested. The presence of each feature is confirmed, denied (e.g., no tear), or inconclusive.

19) whose profile is located within this same azimuth window is best fit by the P12 model. The only observed commonality among the four profiles with variable results between the vertical and radial components is that they all sample the northeastern end of the PE line, which may have implications for the structure of the subduction zone in this corner of the array. Out of the 15 model profiles tested, the slab geometry estimated from the *Cahill and Isacks* (1992) isodepth contours most accurately predicts the observed waveforms along just four profiles. These four profiles (i.e., events 18, 19, 30, and 40) all sample the northern region of the array, near the intersection of the PF and PG lines. Other profiles which sample this same region, however, support the Slab1.0 (*Hayes et al.*, 2012) isodepth contours as a better representation of the slab geometry. Overall, tests of the four possible slab structural features indicate that there is no tear present along either the southeast margin of the projected Nazca Ridge or along the sharpest increase in slab dip, while the presence of the downdip extension of the Nazca Ridge is likely confirmed and the existence of the USL is possible.

The 2D velocity model along the event 26 profile using the preferred P12 velocities is presented in Figure 4.14 as an example. The model is shown with the slab geometry estimated from the isodepth contours of both *Cahill and Isacks* (1992) (Figure 4.14a) and Slab1.0 (*Hayes et al.*, 2012) (Figure 4.14b) for comparison. Data along this transect were recorded by the PG line. This model tests the presence and location of the USL using the lateral extent of the USL zone and its possible extension to the boundary of the no USL zone as shown in Figure 4.13. The synthetics produced from this model, using both possible slab geometries, are compared to the data from three stations in Figure 4.15. A ∼65–70 sec segment of the synthetic waveform that includes the P- and S-wave arrivals is cross-correlated with the data for this segment. The results of this cross-correlation clearly indicate that the Slab1.0 (*Hayes et al.*, 2012) geometry is a better representation of the slab shape along this profile than that derived from *Cahill and Isacks* (1992) (CI). The results from models with the addition of the USL and those that use the MC14 and MC14b velocities are also shown. These models all include the slab geometry estimated from Slab1.0 (*Hayes et al.*, 2012). The lower cross-correlation coefficients for the MC14 and MC14b models relative to those for the P12 model on both the vertical and radial components demonstrate that, out of the three velocity models tested, the P12 velocities are the most accurate representation of the slab structure along this profile. Relative to the model without the USL (P12 in Figure 4.15), the model that includes the USL within the lateral extent of the USL zone, as sampled by this profile (P12_USL; Figure 4.14b), produces improved fits to the data on the radial component at all stations and on the vertical component at some stations. Extending the width of the USL to the boundary of the no USL zone (P12_USL2; Figure 4.14b) produces worse fits to the data relative to the model without the USL on the vertical component at all stations and on the radial component at most stations. Note that stations PG33 and PG35 (Figure 4.15) are the only two stations along the profile which show improved fits on the radial component for the P12_USL2 model. This comparison of modeling results suggests possible confirmation of the presence of the USL, limited to the extent of the USL zone.

The 2D velocity model along the S56°E profile for event 20 using the preferred slab geometry estimated from the isodepth contours of Slab1.0 (*Hayes et al.*, 2012) is shown in Figure 4.16 as an additional example. The model is shown with the P12 (Figure 4.16a) and MC14 (Figure 4.16b) velocities for comparison. The data along this transect were recorded by the PF and PE lines. This model tests the presence of a tear in the slab along the largest transition in dip. As was described for the event 26 model above, the synthetics produced from this model are compared to the data at three stations in Figure 4.17, with cross-correlations between a segment of the synthetic and the data used to assess the quality of fit. Here, the segment used is ∼58–65 sec and still includes the P- and S-wave arrivals. Out of the three sets of velocities tested (i.e., P12, MC14, and MC14b), synthetics produced using the P12 velocities provide the most accurate (overall) prediction of the data on the vertical component, while the same is true for the MC14 velocities on the radial component. Due to this variation between the vertical and radial components, we compare models produced with both of these velocities to those produced with the addition of a tear or with an alternative slab geometry in the following. Consistent with the event 26 results, the cross-correlation coefficients for the event 20 models clearly indicate that the Slab1.0 (*Hayes et al.*, 2012) geometry is a better representation of the slab shape than that derived from *Cahill and Isacks* (1992) (CI). Using this

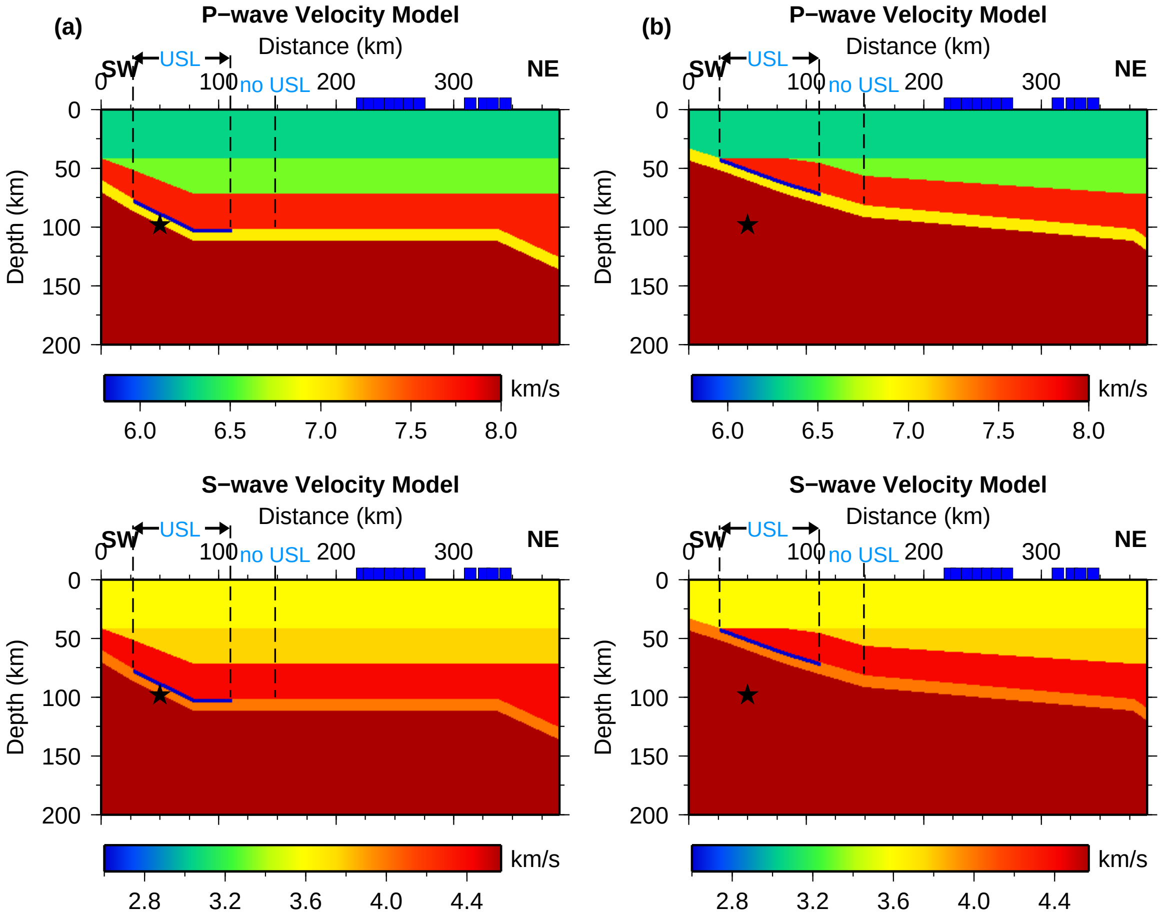

Figure 4.14: 2D velocity models of the subduction zone structure along the PG line (blue squares) for event 26 (Figure 4.13, Table 4.2). P- and S-wave velocities are from the P12 model. Subducted slab shape is estimated from the isodepth contours of (a) *Cahill and Isacks* (1992) and (b) Slab1.0 (*Hayes et al.*, 2012). Note the large variation in slab geometry between (a) and (b). Locations of the USL zone and approximate boundary of the no USL zone are indicated for reference. The location of event 26 used in the modeling is shown by the black star.

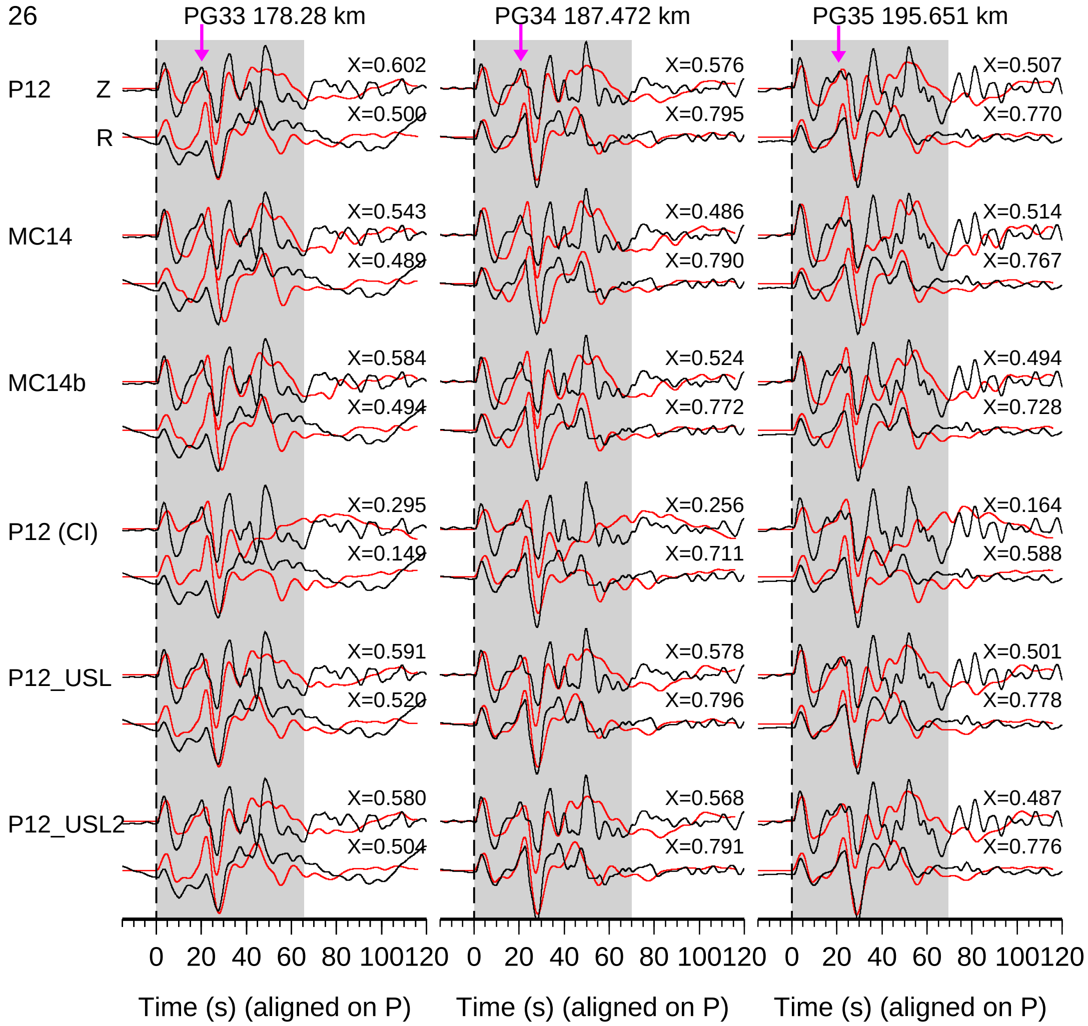

Figure 4.15: Comparison of 2D modeling results of event 26 for six different models at three stations, filtered to 0.01–0.1 Hz. Data are in black, synthetics are in red. Vertical (Z) and radial (R) components are shown. P (dashed line) and S (pink arrow) arrivals are indicated. The top three rows show results using each of the 1D velocity models tested in this study coupled with slab geometry estimated from the Slab1.0 (*Hayes et al.*, 2012) isodepth contours. The P12 (CI) model uses P12 velocities coupled with slab geometry estimated from the *Cahill and Isacks* (1992) (CI) contours. The P12_USL and P12_USL2 models both consist of P12 velocities coupled with slab shape estimated from Slab1.0 and the addition of an USL at the top of the slab. The USL is constrained to the USL zone in P12_USL and extends to the boundary of the no USL zone in P12_USL2 (Figure 4.14b). Cross-correlation coefficients (X) for each model with the data for the grey shaded segment of the waveform are shown. See Table 4.2 for summary of modeling results.

preferred Slab1.0 (*Hayes et al.*, 2012) geometry, models with the addition of 20-km (i.e., P12_dt20 and MC14_dt20) and 50-km (i.e., P12_dt50 and MC14_dt50) wide gaps in the slab centered at the location of the largest transition in slab dip (Figure 4.16) are compared to those without any tearing (i.e., P12 and MC14 in Figure 4.17). The P12_dt20 and MC14_dt20 models provide overall worse fits to the data on both the vertical and radial components than the corresponding models that do not include a tear. The P12_dt50 and MC14_dt50 models both provide slightly improved fits to the data on the vertical component and significantly worse fits on the radial component, which more than counterbalance any improvement on the vertical. As such, these modeling results suggest that there is no tear in the slab along the 8° increase in slab dip.

4.4 Discussion

The transition from flat to normal subduction in southern Peru suggests either tearing or continuous curvature of the subducted Nazca plate to accommodate this change in geometry. In this study, we provide evidence that supports a smooth contortion of the slab based on seismic observations, source mechanism analysis, and modeling of the velocity structure of the subduction zone. Observations of intraslab seismicity reveal a zone of decreased seismicity in the flat slab region, the margin of which is coincident with both the transition to a steeper dip and the intersection of the Nazca Ridge with the Peru-Chile Trench. The decreased seismicity of this zone suggests a change in plate structure, which, coupled with the seismic gap over the projected downdip continuation of the Nazca Ridge, is likely due to the ridge itself. The southward migration of the Nazca Ridge from 11°S since $\sim$11.2 Ma, when it first intersected the trench (*Hampel*, 2002), could explain the observed decrease in seismicity in the flat slab region to the northwest, where the ridge was subducting in the past. Decreased coupling in the seismogenic zone along the current intersection of the Nazca Ridge with the trench implies aseismic creep (*Pritchard and Fielding*, 2008; *Perfettini et al.*, 2010; *Chlieh et al.*, 2011) and may explain the observed downdip gap in intraslab seismicity. While relatively narrow zones of decreased seismicity have been used to suggest plate-tearing in other subduction zones (e.g., *Dougherty and Clayton*, 2014), the broad zone of decreased intermediate depth seismicity observed here is most

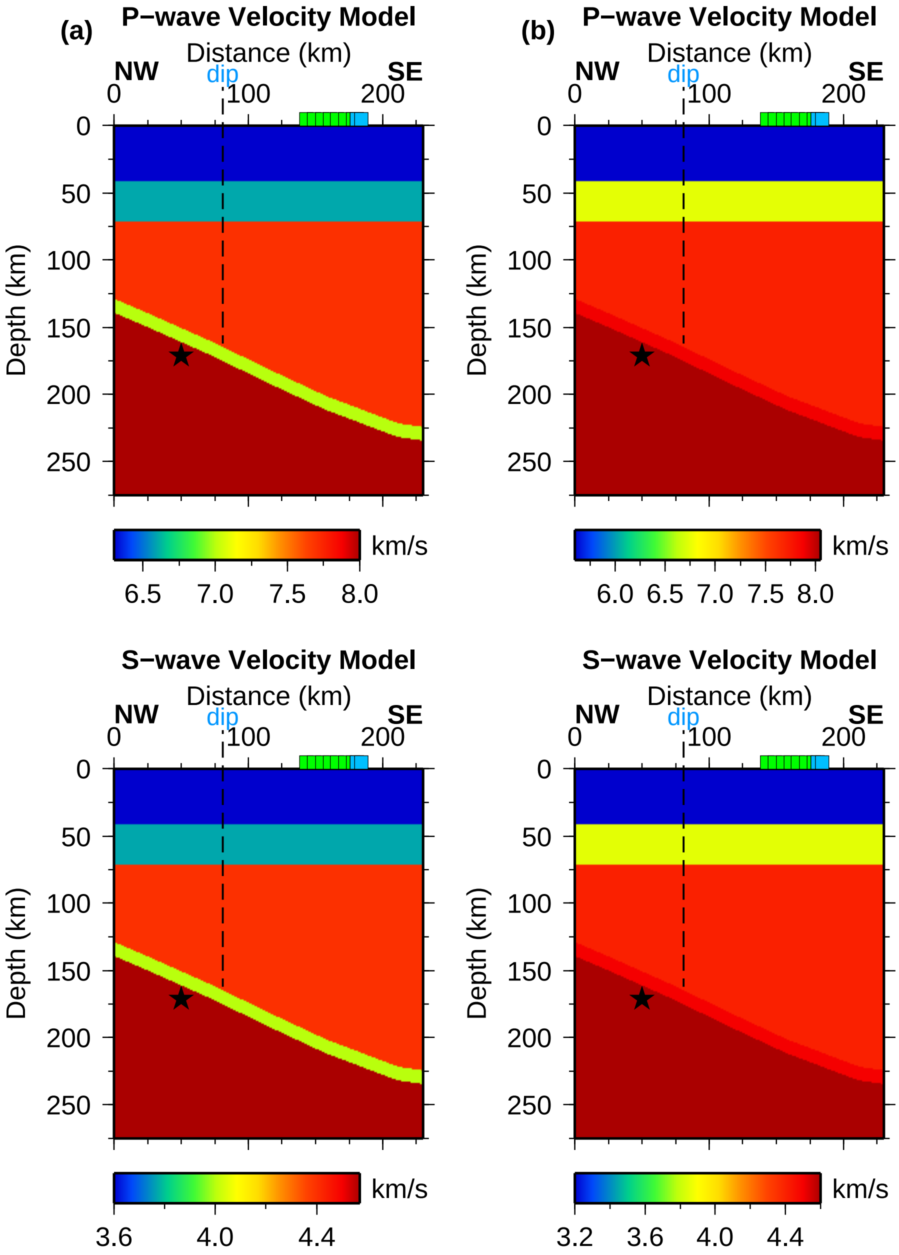

Figure 4.16: 2D velocity models of the subduction zone structure along the PF (green squares) and PE (light blue squares) lines for the S56°E-oriented profile for event 20 (Figure 4.13, Table 4.2). P- and S-wave velocities are from the (a) P12 and (b) MC14 models. Subducted slab shape is estimated from the isodepth contours of Slab1.0 (*Hayes et al.*, 2012). Location of the largest change in slab dip is indicated for reference. The location of event 20 used in the modeling is shown by the black star.

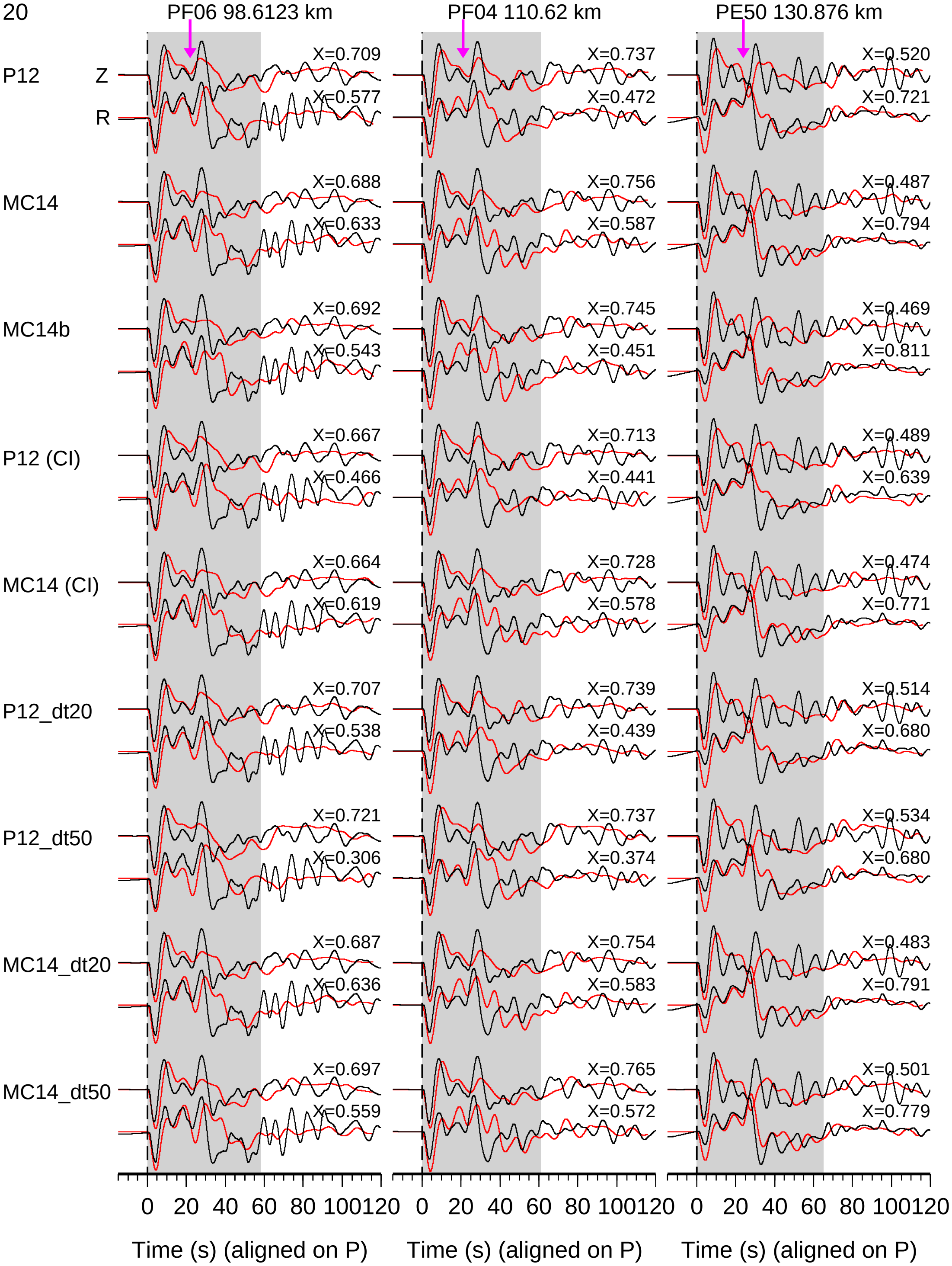

Figure 4.17: Comparison of 2D modeling results of event 20 for nine different models at three stations, filtered to 0.01–0.1 Hz. Data are in black, synthetics are in red. Vertical (Z) and radial (R) components are shown. P (dashed line) and S (pink arrow) arrivals are indicated. The top three rows show results using each of the 1D velocity models tested in this study coupled with slab geometry estimated from the Slab1.0 (*Hayes et al.*, 2012) isodepth contours. The P12 (CI) and MC14 (CI) models use P12 and MC14 velocities, respectively, coupled with slab geometry estimated from the *Cahill and Isacks* (1992) (CI) contours. The P12_dt20 and P12_dt50 models both consist of P12 velocities coupled with slab shape estimated from Slab1.0 and the addition of 20-km and 50-km-wide, respectively, tears (t) in the slab centered at the largest change in dip (d) (Figure 4.16a). Corresponding models using MC14 velocities instead of P12 are also tested (MC14_dt20, MC14_dt50). Cross-correlation coefficients (X) for each model with the data for the grey shaded segment of the waveform are shown. See Table 4.2 for summary of modeling results.

likely due to the subduction of the aseismic Nazca Ridge, not a tear. This is supported by the confirmed projected continuation of the ridge and the lack of slab tear from the 2D finite-difference modeling. The abundant lower crustal seismicity observed within the overriding South American plate in the flat slab region has been suggested to indicate strong coupling between the two plates in this region (e.g., *Barazangi and Isacks*, 1976; *Gutscher*, 2002). If these plates are strongly coupled, however, a higher rate of seismicity would be expected in the flat slab than that observed. In fact, the largest amount of overriding plate seismicity in our study region occurs above the projected linear continuation of the Nazca Ridge, which exhibits low coupling with the South American plate at the trench. This suggests instead that the elevated geometry (∼1.5 km high at the crest (*Woods and Okal*, 1994)) of the subducted Nazca Ridge is imparting increased stress on the base of the overriding plate where the flat slab underplates South America, resulting in increased lower crustal seismicity. This interpretation is consistent with the observed uplift of the Fitzcarrald arch in the Amazonian foreland basin, which is attributed to the projected continuation of the Nazca Ridge (*Espurt et al.*, 2007). The observed cluster of seismicity near the PG line, centered at ∼14°S, 72.85°W, may imply focusing of stress related to the changing slab geometry (*Suárez et al.*, 1990). Its shallower depth range, ∼15–45 km above the estimated slab surface at ∼100 km, suggests possible upwarping of the slab as a flexural response to resubduction downdip and/or lateral contortion. Alternatively, there may be some other (unidentified) localized anomaly responsible for this seismicity cluster; however, shear wave velocities down to 120 km depth reveal no such feature (*Ma and Clayton*, 2014).

Focal mechanisms of the intraslab seismicity elucidate the nature of the flat-to-normal transition in slab dip beyond that of the epicentral ISC catalog locations. The linear ENE-WSW-oriented concentration of events observed along the sharp bend in isodepth contours through the center of the array implies a focusing of stress and increase in seismicity in this region, consistent with plate flexure along a smooth contortion as seen here and elsewhere (*Grange et al.*, 1984b; *McCrory et al.*, 2012). Thrust and oblique faulting mechanisms located at the point of sharpest curvature of the isodepth contours and exhibiting N-S and NW-SE compression indicate the flexural response of the slab around this bend (*Yamaoka et al.*, 1986; *Creager et al.*, 1995; *Kirby et al.*, 1995). Normal faulting mechanisms with NNW-SSE extension located near the intersection of the PE and PF lines to the southeast show further response of the slab to the smooth contortion between flat and normal subduction (*Schneider and Sacks*, 1987; *Tavera and Buforn*, 2001). The N-S and NW-SE extensional mechanisms of the cluster of seismicity near event 38 in Figure 4.1 support our hypothesis that this seismicity may be due to along-strike bending of the slab as the result of a lateral contortion, wherein the more steeply dipping region is sinking and exerting lateral slab-pull on the horizontal section (*Schneider and Sacks*, 1987). Additionally, the lack of observed "tearing events" consisting of steeply dipping focal planes aligned along the strike of a possible tear location (*Gutscher et al.*, 1999b) imply that there is no tear present in southern Peru. The absence of compressional mechanisms in the flat slab region also argues against strong coupling between the Nazca and South American plates, as noted for the ISC data above.

From estimating the lateral variation in slab dip using Wadati-Benioff zone seismicity, we find a gradual increase in slab dip indicative of a smooth contortion in the Nazca plate. Further exploration of this seismicity in the trench-parallel direction reveals no gaps or vertical offsets which might indicate tearing of the plate, consistent with the continuous slab identified from receiver functions (*Phillips and Clayton*, 2014) and imaged tomographically (*Engdahl et al.*, 1995). This is contrary to what has been observed along the flat-to-normal transition in northern Peru/southern Ecuador, where both a gap and vertical offset in seismicity suggest a slab tear (*Gutscher et al.*, 1999b). The 3D surface generated from piecewise-linear regression fits to the seismicity clearly indicates the continuous curvature of the slab from flat to normal subduction in southern Peru, consistent with the confirmed absence of tearing in the 2D modeling results. The anomalous rise in the northwestern corner of the downdip region of the slab surface may be due to decreased seismicity in this region, resulting in fits that are less constrained through this area, producing an anomalous shallowing of the surface. An alternative explanation is that this rise may reflect the flexural bulge of the plate suggested from the observed cluster of shallower seismicity in this region. Such a bulge, however, was not identified from receiver functions (*Phillips and Clayton*, 2014).

Examination of the lateral extent of the USL shows that it is restricted to the flat slab region in the northwest portion of our study area. The observed boundary between the USL (or possible USL) and no USL zones that is coincident with the southeast margin of the projected continuation of the Nazca Ridge suggests a change in plate structure here, as was identified from the observed decrease in seismicity. Similar boundaries in central Mexico were used in conjunction with coincident sharp transitions in slab dip to suggest tearing of the subducted plate (*Dougherty et al.*, 2012; *Dougherty and Clayton*, 2014). In southern Peru, however, this boundary is within the horizontal subduction region and is ~100 km northwest of where the slab ceases to be flat and begins to gradually increase in dip. The lack of a coincident sharp transition in slab dip here suggests that this boundary is not indicating a tear in the slab, but rather is related to a structural change caused by the subduction of the Nazca Ridge. The confirmed absence of a slab tear here from 2D modeling further reinforces this conclusion. The concentration of the USL zone immediately downdip from where the Nazca Ridge intersects the trench suggests that this low strength layer may be responsible for the observed low coupling and gap in intermediate depth seismicity within the projected continuation of the ridge. Such decoupling of the flat slab from the overriding plate has also been observed in central Mexico (*Singh and Pardo*, 1993; *Franco et al.*, 2005) and is attributed to the USL there (*Kim et al.*, 2010). The possibly confirmed presence of the USL zone from 2D modeling also supports this theory; however, further modeling along different profiles and/or using different events would provide additional constraints on the presence of the USL. Previous studies have noted increased hydration of the oceanic lithosphere within the Nazca Ridge evidenced by decreased seismic velocities (*Couch and Whitsett*, 1981; *Ma and Clayton*, 2014) and increased receiver function amplitudes (*Phillips and Clayton*, 2014). This hydration may support the formation of the USL by providing additional free-fluid and/or hydrous minerals to the subduction zone. A possible mechanism for the formation of the USL in this region can be suggested if its composition as a talc-rich ultramafic layer that originated from the mantle wedge (*Kim et al.*, 2013) is assumed.

We propose that the initial subduction of the Nazca Ridge at 11°S introduced additional water to the subduction zone as the slab dehydrated. This increased the localized concentration of water in the mantle wedge, resulting in the production of talc (*Kim et al.*, 2013) overlying the subducted ridge. Talc formation decreases the viscosity of the wedge, which may facilitate flattening of the slab (*Manea and Gurnis*, 2007; *Kim et al.*, 2013). In Peru, the flattening of the Nazca slab is estimated to have begun ∼10–12 Ma (*Ramos and Folguera*, 2009), consistent with the initial subduction of the Nazca Ridge ∼11.2 Ma (*Hampel*, 2002). Partly based on this temporal coincidence, the buoyancy of the ridge is often suggested as a cause of flat subduction in this region (e.g., *Pilger*, 1981; *Soler and Bonhomme*, 1990; *Gutscher et al.*, 1999a); however, geodynamical modeling has demonstrated that the buoyancy of the ridge alone is insufficient to cause flattening of the slab (*van Hunen et al.*, 2004; *Espurt et al.*, 2008; *Gerya et al.*, 2009). Further discussion of possible causes of flat subduction is given in *Gutscher* (2002), *van Hunen et al.* (2004), and *Pérez-Gussinyé et al.* (2008). As the Nazca Ridge migrates southward, continued dehydration introduces an increased concentration of water to a new section of mantle wedge, resulting in talc formation there. Once the ridge migrates, the flux of water into the section of mantle wedge overlying its former location decreases, which decreases or stops talc production. Translating this process into the distribution of the USL, the increased hydration of the Nazca Ridge causes localized formation of the USL along its downdip continuation. Southward migration of the ridge results in a weak or dissipating USL to the northwest due to decreased hydration of the mantle wedge. This interpretation is consistent with the observed USL zone located downdip from the current position of the Nazca Ridge and the possible USL zone located in the flat slab region to the northwest.

The 2D velocity modeling also provides valuable insights into the structure and morphology of the slab along the transition from flat to normal subduction, which can most accurately be described as consisting, overall, of P12 velocity material with Slab1.0 (*Hayes et al.*, 2012) geometry. The failure of the MC14 and MC14b velocities to provide better fits to the data may be the result of oversimplification of the velocity structure imaged by *Ma and Clayton* (2014) for this study. A more complex velocity model that includes the imaged lateral heterogeneity and low velocity zone in the overriding plate (*Ma and Clayton*, 2014) may be more representative of the subduction zone structure. Additionally, the preference of slab geometries estimated from the isodepth contours of Slab1.0 (*Hayes et al.*, 2012) over *Cahill and Isacks* (1992) is puzzling. The *Cahill and Isacks*

(1992) contours are more consistent with the observed Wadati-Benioff zone seismicity than those of Slab1.0 (*Hayes et al.*, 2012), especially in the flat slab region. *Hayes et al.* (2012) even acknowledges their difficulty in fitting the true subduction interface in this region, as evidenced by anomalous short-wavelength features and large misfits. The slab surface as determined from receiver functions (*Phillips et al.*, 2012; *Phillips and Clayton*, 2014) is also more consistent with the *Cahill and Isacks* (1992) contours.

In an effort to understand why smooth contortion of the slab along flat-to-normal transitions occurs in some places and plate tearing in others, we examine the lateral strain of the smoothly contorting Nazca slab in southern Peru and compare it with that of the likely torn Cocos slab in western and eastern central Mexico. Slab dip estimates for western central Mexico (*Dougherty et al.*, 2012), eastern central Mexico (*Dougherty and Clayton*, 2014), and southern Peru (this study) are used to approximate the slab surface in each region along a trench-parallel cross-section (Figure 4.18a). It should be noted that there are only four dip estimates for western central Mexico, while eastern central Mexico and southern Peru have 21 and 17 data points, respectively. Also, the dip estimates for western central Mexico were made from seismicity in 50-km-wide bins, while those in the other two regions utilized 25-km-wide bins. Comparison of the approximate slab surfaces in Figure 4.18a clearly demonstrates the gradual transition from flat to normal subduction in southern Peru relative to the abrupt transitions in both regions of central Mexico. *Dougherty et al.* (2012) and *Dougherty and Clayton* (2014) both noted sharp increases in slab dip of 14°, while the largest increase in slab dip that we observe in southern Peru is only 8° and is preceded by several smaller increases of 3° and 5° across the slab transition. The incremental normal strain between each bin in which a dip estimate is obtained is shown in Figure 4.18b for all three regions. This strain is calculated as the fractional change in length, where the original length is the bin width (i.e., 25 km or 50 km). The largest incremental strain occurs at the sharpest gradient in the slab surface in all three regions, with nearly all of the strain in the Cocos slab concentrated here, while strain in the Nazca slab is distributed over a larger area. In order to compare the overall strain among the three regions on the same length scale, we select a 150-km-wide segment of the eastern central Mexico and southern Peru slabs centered around the midpoint of the largest gradient in the slab surface. The normal strains over this segment are calculated to be ~10% in southern Peru and ~15% in both regions of central Mexico. Other studies also find 10% along-strike strain in this region of southern Peru (*Schneider and Sacks*, 1987; *Creager et al.*, 1995). In central Mexico, *Burbach and Frohlich* (1986) estimate a lateral strain of ~15% in the west and ~6% in the east. The discrepancy between our calculated strain and that of *Burbach and Frohlich* (1986) in eastern central Mexico may be due to the small amount of seismicity in this region that is used in their strain estimation, yielding a less well constrained value. The difference in strain of 5% between southern Peru and central Mexico may partly explain why tearing occurs in the Cocos slab, but not in the Nazca slab; however, other factors are likely also responsible.

Tearing of the young, ~15 Ma in the west and ~18 Ma in the east (*Ferrari et al.*, 2012), Cocos slab and not of the much older, ~45 Ma (*Müller et al.*, 2008), Nazca slab is counterintuitive, even with an increase in strain of 5%. Young slabs are warmer and generally show less resistance against bending relative to their older counterparts (*van Hunen et al.*, 2002), suggesting that a smooth contortion would be more likely to occur in a young slab, while an older slab would be more likely to fail and tear. One possible explanation is that rollback of the Cocos slab since the late Miocene (*Ferrari et al.*, 2012) imposed stresses on the slab which resulted in tearing along pre-existing lines of weakness in the subducting plate located at the transitions from flat to normal subduction (*Dougherty and Clayton*, 2014), where the slab was previously contorted. These lines of weakness include the projected extension of the Orozco Fracture Zone in the west (*Bandy et al.*, 2000; *Dougherty et al.*, 2012; *Stubailo et al.*, 2012) and parallel ridges of seamounts in the east (*Dougherty and Clayton*, 2014). The absence of similar rollback and of a coincident line of weakness at the slab transition in southern Peru supports the Nazca slab remaining continuous.

4.5 Conclusions

The nature of the transition from flat to normal subduction in southern Peru is investigated using intraslab seismicity patterns, focal mechanism orientations, an analysis of P waveform complexities,

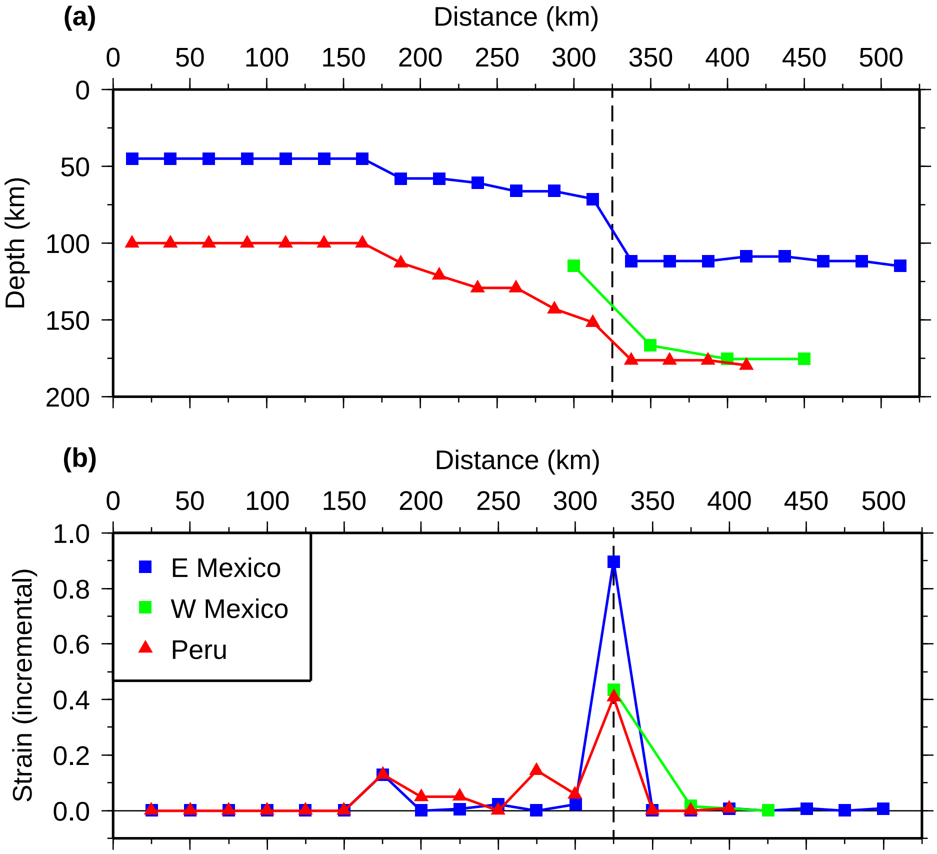

Figure 4.18: Slab strain along the transition from flat to normal subduction in three regions. (a) Depth to the top of the slab using slab dip estimates for eastern central Mexico (*Dougherty and Clayton*, 2014), western central Mexico (*Dougherty et al.*, 2012), and southern Peru (this study). Slabs are aligned along midpoint of largest gradient in depth (black dashed line). Note the gradual transition from flat (left) to normal (right) subduction in southern Peru relative to the abrupt transitions in both regions of central Mexico. (b) Incremental strain between each bin in which a dip estimate is obtained. Bins in eastern central Mexico and southern Peru are 25 km wide; those in western central Mexico are 50 km wide.

and 2D waveform modeling techniques. The results show that the subducted Nazca plate is a complicated structure with a possible thin USL atop the horizontal slab. The lateral extent of this USL is coincident with the margin of the projected continuation of the subducting Nazca Ridge, implying a change in structure which we interpret as a causal relationship between these features. A gradual increase in slab dip with no sharp transitions suggests smooth contortion of the Nazca plate. The lack of any gaps or vertical offsets in the intraslab seismicity coupled with the concentration and orientation of focal mechanisms indicative of slab bending further support this conclusion. The absence of a tear in the slab along either the Nazca Ridge or the largest increase in slab dip is also confirmed with 2D waveform modeling. Further modeling of the subduction zone structure in the flat slab region may provide additional constraints on the presence of the USL.

4.6 Supplemental Figures

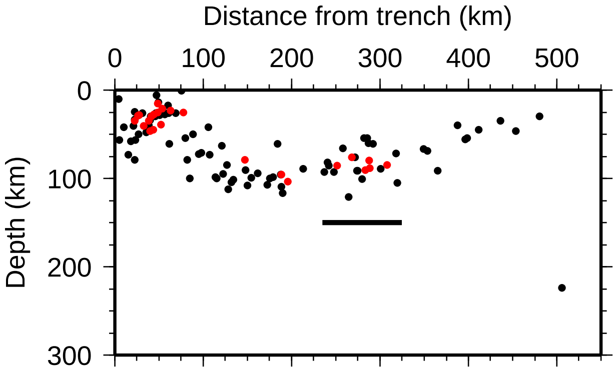

Figure 4.19: Trench-normal cross-section of seismicity from the 1960–2013 ISC Bulletin event catalog (*International Seismological Centre*, 2011) (black dots) in bin 3 of Figure 4.5. Hypocenter locations for earthquakes from the relocated 1960–2008 EHB Bulletin event catalog (*International Seismological Centre*, 2011) (red dots) are shown for reference. A black horizontal bar marks the location of the shallower cluster of seismicity centered at ∼14°S, 72.85°W that was noted for Figure 4.3.

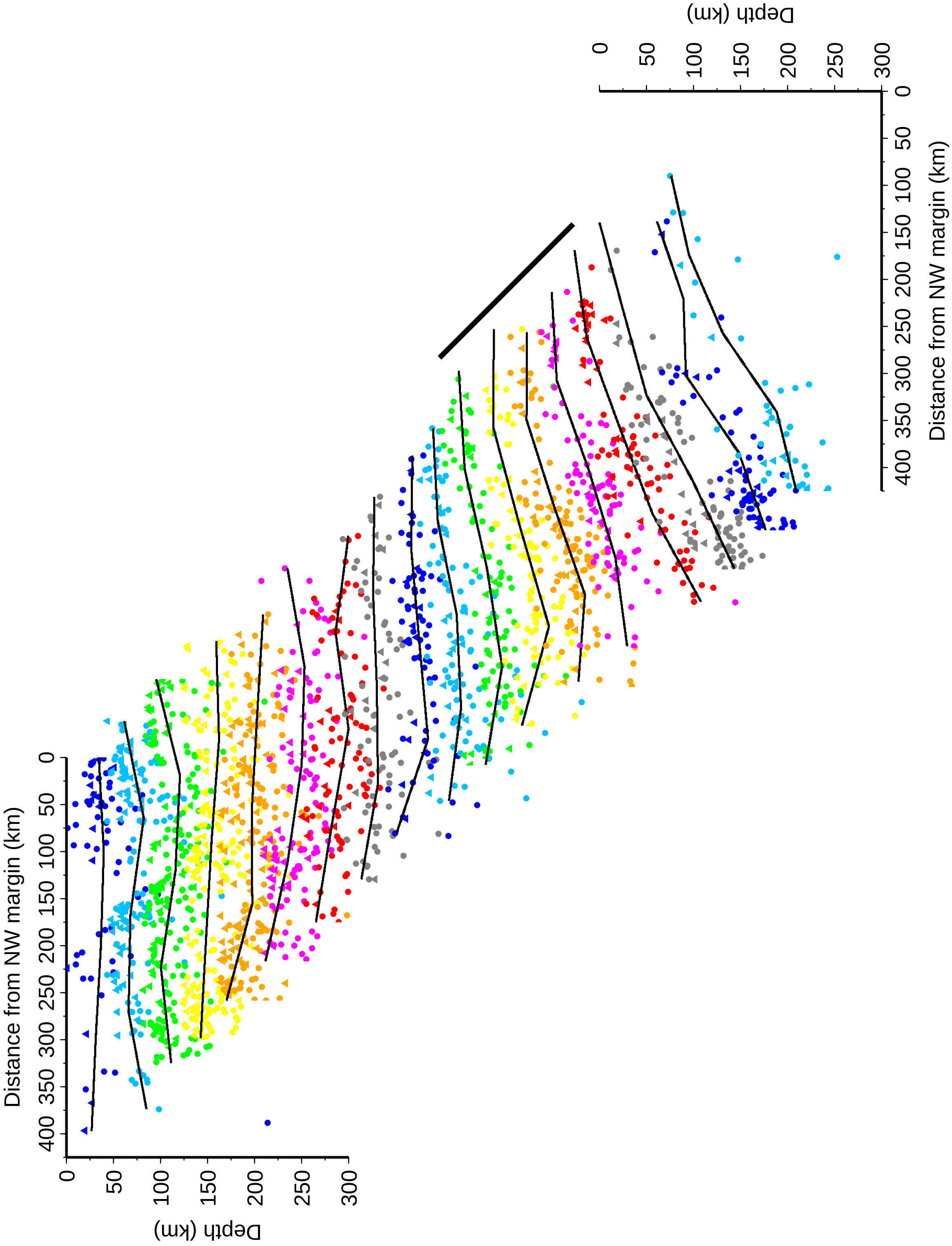

Figure 4.20: Perspective view (updip) of cross-sections of slab seismicity from the ISC (dots) and EHB (triangles) catalogs in trench-parallel bins h1 (top) to h18 (bottom; see Figure 4.6 for bin locations). Events within the overriding plate are not shown. All events within a particular bin are shown as a single color. Variations in color between bins are used to distinguish cross-sections. Weighted piecewise-linear regression fits to the slab seismicity in each cross-section are shown (black lines). Cross-sections for bins h11–h15 shown in Figure 4.7 are marked by a heavy black line. Note the abrupt step in the fit for bin h17 due to a poorly constrained regression from sparse data in this bin.

References

Bandy, W. L., T. W. C. Hilde, and C.-Y. Yan (2000), The Rivera-Cocos plate boundary: Implications for Rivera-Cocos relative motion and plate fragmentation, in *Cenozoic Tectonics and Volcanism of Mexico*, *Geol. Soc. Am. Spec. Pap.*, vol. 334, edited by H. Delgado-Granados, G. Aguirre-Díaz, and J. M. Stock, pp. 1–28, GSA, Boulder, Colorado.

Barazangi, M., and B. L. Isacks (1976), Spatial distribution of earthquakes and subduction of the Nazca plate beneath South America, *Geology*, *4*, 686–692.

Barazangi, M., and B. L. Isacks (1979), Subduction of the Nazca plate beneath Peru: evidence from spatial distribution of earthquakes, *Geophys. J. R. astr. Soc.*, *57*, 537–555.

Bevis, M., and B. L. Isacks (1984), Hypocentral trend surface analysis: Probing the geometry of Benioff zones, *J. Geophys. Res.*, *89*, 6153–6170.

Boyd, T. M., J. A. Snoke, I. S. Sacks, and A. R. B. (1984), High-resolution determination of the Benioff zone geometry beneath southern Peru, *Bull. Seis. Soc. Am.*, *74*, 559–568.

Burbach, G. V., and C. Frohlich (1986), Intermediate and deep seismicity and lateral structure of subducted lithosphere in the circum-Pacific region, *Rev. Geophys.*, *24*, 833–874.

Cahill, T., and B. L. Isacks (1992), Seismicity and shape of the subducted Nazca Plate, *J. Geophys. Res.*, *97*, 17,503–17,529.

Chlieh, M., H. Perfettini, H. Tavera, J.-P. Avouac, D. Remy, J.-M. Nocquet, F. Rolandone, F. Bondoux, G. Gabalda, and S. Bonvalot (2011), Interseismic coupling and seismic potential along the Central Andes subduction zone, *J. Geophys. Res.*, *116*, B12405, doi:10.1029/2010JB008166.

Couch, R., and R. M. Whitsett (1981), Structures of the Nazca Ridge and the continental shelf and slope of southern Peru, in *Nazca Plate: Crustal Formation and Andean Convergence*, *Geol. Soc. Am. Mem.*, vol. 154, edited by L. D. Kulm, J. Dymond, E. J. Dasch, D. M. Hussong, and R. Roderick, pp. 569–586, GSA, Boulder, Colorado.

Creager, K. C., L.-Y. Chiao, J. P. Winchester, and E. R. Engdahl (1995), Membrane strain rates in the subducting plate beneath South America, *Geophys. Res. Lett.*, *22*, 2321–2324.

DeMets, C., R. G. Gordon, and D. F. Argus (2010), Geologically current plate motions, *Geophys. J. Int.*, *181*, 1–80, doi:10.1111/j.1365-246X.2009.04491.x.

D'Errico, J. (2005), *Surface fitting using gridfit*, MATLAB Central File Exchange, http://www.mathworks.com/matlabcentral/fileexchange/8998-surface-fitting-using-gridfit, accessed 18 April 2014.

D'Errico, J. (2009), *SLM - Shape Language Modeling*, MATLAB Central File Exchange, http://www.mathworks.com/matlabcentral/fileexchange/24443-slm-shape-language-modeling, accessed 17 April 2014.

Dougherty, S. L., and R. W. Clayton (2014), Seismicity and structure in central Mexico: Evidence for a possible slab tear in the South Cocos plate, *J. Geophys. Res.*, *119*, 3424–3447, doi: 10.1002/2013JB010883.

Dougherty, S. L., R. W. Clayton, and D. V. Helmberger (2012), Seismic structure in central Mexico: Implications for fragmentation of the subducted Cocos plate, *J. Geophys. Res.*, *117*, B09316, doi:10.1029/2012JB009528.

Dziewonski, A. M., T.-A. Chou, and J. H. Woodhouse (1981), Determination of earthquake source parameters from waveform data for studies of global and regional seismicity, *J. Geophys. Res.*, *86*, 2825–2852, doi:10.1029/JB086iB04p02825.

Ekström, G., M. Nettles, and A. M. Dziewonski (2012), The global CMT project 2004-2010: Centroid-moment tensors for 13,017 earthquakes, *Phys. Earth Planet. Inter.*, *200-201*, 1–9, doi: 10.1016/j.pepi.2012.04.002.

Engdahl, E. R., R. D. van der Hilst, and J. Berrocal (1995), Imaging of subducted lithosphere beneath South America, *Geophys. Res. Lett.*, *22*, 2317–2320.

Espurt, N., P. Baby, S. Brusset, M. Roddaz, W. Hermoza, V. Regard, P.-O. Antoine, R. Salas-Gismondi, and R. Bolaños (2007), How does the Nazca Ridge subduction influence the modern Amazonian foreland basin?, *Geology*, *35*, 515–518, doi:10.1130/G23237A.1.

Espurt, N., F. Funiciello, J. Martinod, B. Guillaume, V. Regard, C. Faccenna, and S. Brusset (2008), Flat subduction dynamics and deformation of the South American plate: Insights from analog modeling, *Tectonics*, *27*, TC3011.

Farr, T. G., P. A. Rosen, E. Caro, R. Crippen, R. Duren, S. Hensley, M. Kobrick, M. Paller, E. Rodriguez, L. Roth, D. Seal, S. Shaffer, J. Shimada, J. Umland, M. Werner, M. Oskin, D. Burbank, and D. Alsdorf (2007), The Shuttle Radar Topography Mission, *Rev. Geophys.*, *45*, RG2004, doi:10.1029/2005RG000183.

Ferrari, L., T. Orozco-Esquivel, V. Manea, and M. Manea (2012), The dynamic history of the Trans-Mexican Volcanic Belt and the Mexico subduction zone, *Tectonophysics*, *522-523*, 122–149, doi:10.1016/j.tecto.2011.09.018.

Franco, S. I., V. Kostoglodov, K. M. Larson, V. C. Manea, M. Manea, and J. A. Santiago (2005), Propagation of the 2001-2002 silent earthquake and interplate coupling in the Oaxaca subduction zone, Mexico, *Earth Planets Space*, *57*, 973–985.

Gerya, T. V., D. Fossati, C. Cantieni, and D. Seward (2009), Dynamic effects of aseismic ridge subduction: numerica modelling, *Eur. J. Mineral.*, *21*, 649–661.

Grange, F., P. Cunningham, J. Gagnepain, D. Hatzfeld, P. Molnar, L. Ocola, A. Rodrígues, S. W. Roecker, J. M. Stock, and G. Suárez (1984a), The configuration of the seismic zone and the downgoing slab in southern Peru, *Geophys. Res. Lett.*, *11*, 38–41.

Grange, F., D. Hatzfeld, P. Cunningham, P. Molnar, S. W. Roecker, G. Suárez, A. Rodrígues, and L. Ocola (1984b), Tectonic implications of the microearthquake seismicity and fault plane solutions in southern Peru, *J. Geophys. Res.*, *89*, 6139–6152.

Gutscher, M.-A. (2002), Andean subduction styles and their effect on thermal structure and interplate coupling, *J. South Am. Earth Sci.*, *15*, 3–10.

Gutscher, M.-A., J.-L. Olivet, D. Aslanian, J.-P. Eissen, and R. Maury (1999a), The "lost Inca Plateau": cause of flat subduction beneath Peru?, *Earth Planet. Sci. Lett.*, *171*, 335–341.

Gutscher, M.-A., J. Malavieille, S. Lallemand, and J.-Y. Collot (1999b), Tectonic segmentation of the North Andean margin: impact of the Carnegie Ridge collision, *Earth Planet. Sci. Lett.*, *168*, 255–270.

Hampel, A. (2002), The migration history of the Nazca Ridge along the Peruvian active margin: a re-evaluation, *Earth Planet. Sci. Lett.*, *203*, 665–679.

Hasegawa, A., and I. S. Sacks (1981), Subduction of the Nazca plate beneath Peru as determined from seismic observations, *J. Geophys. Res.*, *86*, 4971–4980.

Hayes, G. P., D. J. Wald, and R. L. Johnson (2012), Slab1.0: A three-dimensional model of global subduction zone geometries, *J. Geophys. Res.*, *117*, B01302.

International Seismological Centre (2011), *On-line Bulletin*, Int. Seis. Cent., Thatcham, United Kingdom, http://www.isc.ac.uk.

Kim, Y., R. W. Clayton, and J. M. Jackson (2010), Geometry and seismic properties of the subducting Cocos plate in central Mexico, *J. Geophys. Res.*, *115*, B06310, doi:10.1029/2009JB006942.

Kim, Y., R. W. Clayton, P. D. Asimow, and J. M. Jackson (2013), Generation of talc in the mantle wedge and its role in subduction dynamics in central Mexico, *Earth Planet. Sci. Lett.*, *384*, 81–87, doi:10.1016/j.epsl.2013.10.006.

Kirby, S. H., E. A. Okal, and E. R. Engdahl (1995), The 9 June 94 Bolivian deep earthquake: An exceptional event in an extraordinary subduction zone, *Geophys. Res. Lett.*, *22*, 2233–2236.

Ma, Y., and R. W. Clayton (2014), The crust and uppermost mantle structure of Southern Peru from ambient noise and earthquake surface wave analysis, *Earth Planet. Sci. Lett.*, *395*, 61–70.

Manea, V., and M. Gurnis (2007), Subduction zone evolution and low viscosity wedges and channels, *Earth Planet. Sci. Lett.*, *264*, 22–45, doi:10.1016/j.epsl.2007.08.030.

Manea, V. C., M. Manea, V. Kostoglodov, C. A. Currie, and G. Sewell (2004), Thermal structure, coupling and metamorphism in the Mexican subduction zone beneath Guerrero, *Geophys. J. Int.*, *158*, 775–784, doi:10.1111/j.1365-246X.2004.02325.x.

Manea, V. C., M. Manea, and L. Ferrari (2013), A geodynamical perspective on the subduction of Cocos and Rivera plates beneath Mexico and Central America, *Tectonophysics*, *609*, 56–81, doi:10.1016/j.tecto.2012.12.039.

McCrory, P. A., J. L. Blair, F. Waldhauser, and D. H. Oppenheimer (2012), Juan de Fuca slab geometry and its relation to Wadati-Benioff zone seismicity, *J. Geophys. Res.*, *117*, B09306, doi: 10.1029/2012JB009407.

Müller, R. D., M. Sdrolias, C. Gaina, and W. R. Roest (2008), Age, spreading rates, and spreading symmetry of the world's ocean crust, *Geochem. Geophys. Geosyst.*, *9*, Q04006.

Pérez-Gussinyé, M., A. R. Lowry, J. P. Morgan, and A. Tassara (2008), Effective elastic thickness variations along the Andean margin and their relationship to subduction geometry, *Geochem. Geophys. Geosyst.*, *9*, Q02003.

Perfettini, H., J.-P. Avouac, H. Tavera, A. Kositsky, J.-M. Nocquet, F. Bondoux, M. Chlieh, A. Sladen, L. Audin, D. L. Farber, and P. Soler (2010), Seismic and aseismic slip on the Central Peru megathrust, *Nature*, *465*, 78–81.

PeruSE (2013), Peru Subduction Experiment, Caltech, dataset, doi:10.7909/C3H41PBZ.

Pesicek, J. D., E. R. Engdahl, C. H. Thurber, H. R. DeShon, and D. Lange (2012), Mantle subducting slab structure in the region of the 2010 M8.8 Maule earthquake (30-40°S), Chile, *Geophys. J. Int.*, *191*, 317–324, doi:10.1111/j.1365-246X.2012.05624.x.

Phillips, K., and R. W. Clayton (2014), Structure of the subduction transition region from seismic array data in southern Peru, *Geophys. J. Int.*, *196*, 1889–1905.

Phillips, K., R. W. Clayton, P. Davis, H. Tavera, R. Guy, S. Skinner, I. Stubailo, L. Audin, and V. Aguilar (2012), Structure of the subduction system in souther Peru from seismic array data, *J. Geophys. Res.*, *117*, B11306, doi:10.1029/2012JB009540.

Pilger, R. H. (1981), Plate reconstructions, aseismic ridges, and low-angle subduction beneath the Andes, *Geol. Soc. Am. Bull.*, *92*, 448–456.

Pilger, R. H., and D. W. Handschumacher (1981), The fixed-hotspot hypothesis and origin of the Easter-Sala y Gomez-Nazca trace, *Geol. Soc. Am. Bull.*, *92*, 437–446.

Pritchard, M. E., and E. J. Fielding (2008), A study of the 2006 and 2007 earthquake sequence of Pisco, Peru, with InSAR and teleseismic data, *Geophys. Res. Lett.*, *35*, L09308.

Ramos, V. A., and A. Folguera (2009), Andean flat-slab subduction through time, in *Ancient Orogens and Modern Analogues*, *Geol. Soc. London Spec. Pub.*, vol. 327, edited by J. B. Murphy, J. D. Keppie, and A. J. Hynes, pp. 31–54, GSL.

Ray, J. S., J. J. Mahoney, R. A. Duncan, J. Ray, P. Wessel, and D. F. Naar (2012), Chronology and geochemistry of lavas from the Nazca Ridge and Easter Seamount Chain: an ∼30 myr hotspot record, *J. Petrol.*, *53*, 1417–1448, doi:10.1093/petrology/egs021.

Schneider, J. F., and I. S. Sacks (1987), Stress in the contorted Nazca plate beneath southern Peru from local earthquakes, *J. Geophys. Res.*, *92*, 13,887–13,902.

Singh, S. K., and M. Pardo (1993), Geometry of the Benioff zone and state of stress in the overriding plate in central Mexico, *Geophys. Res. Lett.*, *20*, 1483–1486.

Smith, W. H. F., and D. T. Sandwell (1997), Global seafloor topography from satellite altimetry and ship depth soundings, *Science*, *277*, 1957–1962.

Soler, P., and M. G. Bonhomme (1990), Relation of magmatic activity to plate dynamics in central Peru from Late Cretaceous to present, in *Plutonism from Antarctica to Alaska*, *Geol. Soc. Am. Spec. Pap.*, vol. 241, edited by S. M. Kay and C. W. Rapela, pp. 173–192, GSA, Boulder, Colorado.

Song, T. A., and Y. Kim (2012), Anisotropic uppermost mantle in young subducted slab underplating Central Mexico, *Nature Geosci.*, *5*, 55–59, doi:10.1038/NGEO1342.

Song, T. A., D. V. Helmberger, M. R. Brudzinski, R. W. Clayton, P. Davis, X. Pérez-Campos, and S. K. Singh (2009), Subducting slab ultra-slow velocity layer coincident with silent earthquakes in southern Mexico, *Science*, *324*, 502–506.

Stubailo, I., C. Beghein, and P. M. Davis (2012), Structure and anisotropy of the Mexico subduction zone based on Rayleigh-wave analysis and implications for the geometry of the Trans-Mexican Volcanic Belt, *J. Geophys. Res.*, *117*, B05303, doi:10.1029/2011JB008631.

Suárez, G., J. Gagnepain, A. Cisternas, D. Hatzfeld, P. Molnar, L. Ocola, S. W. Roecker, and J. P. Viodé (1990), Tectonic deformation of the Andes and the configuration of the subducted slab in central Peru: results from a microseismic experiment, *Geophys. J. Int.*, *103*, 1–12.

Tavera, H., and E. Buforn (2001), Source mechanism of earthquakes in Peru, *J. Seis.*, *5*, 519–539.

van Hunen, J., A. P. van den Berg, and N. J. Vlaar (2002), On the role of subducting oceanic plateaus in the development of shallow flat subduction, *Tectonophysics*, *352*, 317–333.

van Hunen, J., A. P. van den Berg, and N. J. Vlaar (2004), Various mechanisms to induce present-day shallow flat subduction and implications for the younger Earth: a numerical parameter study, *Phys. Earth Planet. Int.*, *146*, 179–194.

Vogt, P. R., A. Lowrie, D. R. Bracey, and R. N. Hey (1976), *Subduction of Aseismic Oceanic Ridges: Effects on Shape, Seismicity, and Other Characteristics of Consuming Plate Boundaries*, *Geol. Soc. Am. Spec. Pap.*, vol. 172, GSA, Boulder, Colorado.

von Huene, R., I. A. Pecher, and M.-A. Gutscher (1996), Development of the accretionary prism along Peru and material flux after subduction of Nazca Ridge, *Tectonics*, *15*, 19–33.

Ward, K. M., R. C. Porter, G. Zandt, S. L. Beck, L. S. Wagner, E. Minaya, and H. Tavera (2013), Ambient noise tomography across the Central Andes, *Geophys. J. Int.*, *194*, 1559–1573.

Woods, M. T., and E. A. Okal (1994), The structure of the Nazca ridge and Sala y Gomez seamount chain from the dispersion of Rayleigh waves, *Geophys. J. Int.*, *117*, 205–222.

Yamaoka, K., Y. Fukao, and M. Kumazawa (1986), Spherical shell tectonics: Effects of sphericity and inextensibility of the geometry of the descending lithosphere, *Rev. Geophys.*, *24*, 27–53.